Atmospheric Environment 214 (2019) 116824

Contents lists available at ScienceDirect

Atmospheric Environment

journal homepage: www.elsevier.com/locate/atmosenv

Retrieval of optical and microphysical properties of transported Saharan dust over Athens and Granada based on multi-wavelength Raman lidar measurements: Study of the mixing processes

O. Soupiona[a,*], S. Samaras[b,e], P. Ortiz-Amezcua[c,d], C. Böckmann[e], A. Papayannis[a], G.A. Moreira[c,d,f], J.A. Benavent-Oltra[c,d], J.L. Guerrero-Rascado[c,d], A.E. Bedoya-Velásquez[c,d,g], F.J. Olmo[c,d], R. Román[c,d,h], P. Kokkalis[i], M. Mylonaki[a], L. Alados-Arboledas[c,d], C.A. Papanikolaou[a], R. Foskinis[a]

[a] Laser Remote Sensing Unit, Physics Department, School of Applied Mathematics and Physical Sciences, National Technical University of Athens, 15780, Zografou, Greece
[b] German Aerospace Center (DLR), German Remote Sensing Datacenter (DFD), Wessling, Germany
[c] Andalusian Institute for Earth System Research (IISTA-CEAMA), 18006, Granada, Spain
[d] Department of Applied Physics, University of Granada, 18071, Granada, Spain
[e] Institute of Mathematics, Potsdam University, 14469, Potsdam, Germany
[f] Institute of Research and Nuclear Energy (IPEN), São Paulo, Brazil
[g] Sciences Faculty, Department of Physics, Universidad Nacional de Colombia, Medellín, Colombia
[h] Grupo de Óptica Atmosférica (GOA), Universidad de Valladolid, Paseo Belén, 7, 47011, Valladolid, Spain
[i] Department of Physics, Kuwait University, P.O. Box 5969, Safat, 13060, Kuwait

A B S T R A C T

In this paper we extract the aerosol microphysical properties for a collection of mineral dust cases measured by multi-wavelength depolarization Raman lidar systems located at the National Technical University of Athens (NTUA, Athens, Greece) and the Andalusian Institute for Earth System Research (IISTA-CEAMA, Granada, Spain). The lidar-based retrievals were carried out with the Spheroidal Inversion eXperiments software tool (SphInX) developed at the University of Potsdam (Germany). The software uses regularized inversion of a two-dimensional enhancement of the Mie model based on the spheroid-particle approximation with the aspect ratio determining the particle shape. The selection of the cases was based on the transport time from the source regions to the measuring sites. The aerosol optical depth as measured by AERONET ranged from 0.27 to 0.54 (at 500 nm) depending on the intensity of each event. Our analysis showed the hourly mean particle linear depolarization ratio and particle lidar ratio values at 532 nm ranging from 11 to 34% and from 42 to 79 sr respectively, depending on the mixing status, the corresponding air mass pathways and their transport time. Cases with shorter transport time showed good agreement in terms of the optical and SphInX-retrieved microphysical properties between Athens and Granada providing a complex refractive index value equal to 1.4 + 0.004i. On the other hand, the results for cases with higher transport time deviated from the aforementioned ones as well as from each other, providing, in particular, an imaginary part of the refractive index ranging from 0.002 to 0.005. Reconstructions of two-dimensional shape-size distributions for each selected layer showed that the dominant effective particle shape was prolate with diverse spherical contributions. The retrieved volume concentrations reflect overall the intensity of the episodes.

1. Introduction

Mineral dust particles have a great impact on the Earth's radiation budget, directly by scattering and absorbing the solar and terrestrial (thermal) radiation and indirectly by acting as cloud condensation nuclei (CCN) and/or ice nuclei (IN), thus, influencing clouds' optical and microphysical properties as well as their lifetimes (Forster et al., 2007; Atkinson et al., 2013; IPCC, 2013; Mamouri and Ansmann, 2015; Seinfeld et al., 2016; Karydis et al., 2017). The Saharan desert is considered as the Earth's largest source of mineral dust (Prospero et al., 2002; Washington et al., 2003). In the regions neighboring this desert, the presence of mineral dust reveals air transport due to favorable environmental conditions for cyclone activity of the air masses (Prospero, 1996; Dunion and Velden, 2004; Gkikas et al., 2015). However, desert dust in most of the cases is not just a mixture of mineral components, but of other components too. This is because anthropogenic and marine air masses mainly from local and long-range pollution are frequently mixed to air masses dominated by mineral dust (Kallos, 1998; Valenzuela et al., 2014a,b).

Dust transport events over the Mediterranean region are usually observed over southern Europe due to cyclone winds (Escudero et al., 2005; Kallos et al., 2006; Guerrero-Rascado et al., 2008; Schepanski and

* Corresponding author.
E-mail address: soupiona.rania@gmail.com (O. Soupiona).

https://doi.org/10.1016/j.atmosenv.2019.116824
Received 4 December 2018; Received in revised form 12 June 2019; Accepted 4 July 2019
Available online 05 July 2019
1352-2310/ © 2019 Elsevier Ltd. All rights reserved.

Knippertz, 2011; Fiedler et al., 2014; Flaounas et al., 2015) and seem to have an increasing trend over the last decades (Ganor et al., 2010; Knippertz and Todd, 2012). There is a clear difference between Eastern and Western Mediterranean dust outbreaks as was pointed out in previous studies (Ganor et al., 2010; Gkikas et al., 2009). In the Western Mediterranean the African dust occurrence is higher in summer (Salvador et al., 2014), while conventional meteorological mechanisms (low pressure systems) provoke a rapid transport of dust towards the Eastern Mediterranean, usually from spring to autumn (Papayannis et al., 2008). More specifically, these three seasons of increased atmospheric dust are summarized in March–May, June–August and September–October as shown by Papayannis et al. (2008) and Soupiona et al. (2018).

Research focusing on the aerosol optical and microphysical properties is needed since these properties change rapidly in processes of aging and mixing (e.g. coagulation, humidification, scavenging by precipitation, particle phase conversion). Due to the diversity of these processes and the different aging degrees, there are still large uncertainties in aerosol microphysical properties. For this purpose, long-term measurements and analyses have been performed in previous years (Balis et al., 2004; Amiridis et al., 2005; Papayannis et al., 2005; Lyamani et al., 2005, 2006a,b, 2008; Mona et al., 2006; Pérez et al., 2006; Papayannis et al., 2008; Preiβler et al., 2013; Soupiona et al., 2018).

Light detection and ranging (lidar) instruments are among the most powerful and suitable tools for retrieving vertically the aerosol optical properties with high temporal and spatial resolution (Balis et al., 2006; Mattis et al., 2008; Mona et al., 2012; Zuev et al., 2017). The particle extinction (α_{aer}) and backscatter coefficients (β_{aer}) and its derived products [lidar ratio (LR), backscatter-related and extinction-related Ångström exponent (AE_β and AE_α), ratio of lidar ratios (LR_{532}/LR_{355})] in various wavelengths are commonly used for aerosol typing (Müller et al., 2007; Groβ et al., 2011; Burton et al., 2012; Groβ S., 2013;; Nicolae et al., 2013; Burton et al., 2015; Groβ et al., 2015) as they are related to particle size and composition. The lidar depolarization technique (Sassen, 2005) is also used for aerosol typing, since it provides information about the non-sphericity of the studied particles. Moreover, Böckmann and Osterloh (2014), based on simulations, showed that depolarization measurements play a crucial role for the derivation of the microphysical properties of irregularly-shaped particles, like mineral dust. The retrieval of these microphysical properties is possible by using combined optical data-sets as inputs in mathematical inversion codes based on regularization of the resulting ill-posed problem (see e.g. Böckmann et al., 2005; Samaras et al., 2015; Veselovskii et al., 2016; Müller et al., 2016).

In this study we show the great potential of lidar stand-alone retrievals of non-spherical aerosol microphysical properties. The main aim of this work is to present the aerosol optical and microphysical properties during selected Saharan dust events over Athens (Greece; NE Mediterranean) and Granada (Spain; NW Mediterranean) focusing on short range to long range dust processes. We selected specific dust transport cases that were interesting in our records regarding their transport time and mixing process whose datasets allowed for stable microphysical inversions. A general description of the instrumentation used is given in Section 2, while section 3 gives a brief description of the Spheroidal Inversion eXperiments (SphInX) software tool. Section 4 describes the criteria for the selection and air mass classification of the four dust cases presented. Section 5 is mainly devoted to the results of the mineral dust optical and microphysical properties retrieved over the two aforementioned stations. Section 6 summarizes this work.

2. Measurement sites and instrumentation

Athens and Granada stations are included in the network of i) EARLINET (since 2000 and 2004 respectively) in compliance with the network's quality assurance criterions and standards, both at the hardware and software levels (Böckmann et al., 2004; Matthais et al., 2004; Freudenthaler, 2008; Pappalardo et al., 2014) and ii) AERONET (since 2008 and 2002 respectively). For nighttime measurements, used in this study from both stations, the Raman technique is applied as proposed by Papayannis et al. (1990) and Ansmann et al. (1992) to retrieve the α_{aer} and β_{aer} vertical profiles, with systematic uncertainties of ~5–15% and ~10–25% respectively (Ansmann et al., 1992; Mattis et al., 2002). Therefore, the corresponding systematic uncertainty of the retrieved lidar ratio values is of order ~11–30%, while the mean uncertainty for AE_α and AE_β is of order 7–21% and 14–35% respectively (Kokkalis et al., 2012).

2.1. Athens Raman lidar depolarization system (EOLE)

The multiwavelength Raman lidar system EOLE (aErosol and Ozone Lidar systEm) of the National Technical University of Athens (NTUA, 37.97° N, 23.79° E, elev. 212 m a.s.l.) is located at the Laser Remote Sensing Unit (LRSU) of NTUA. Its emission unit is based on a Nd:YAG laser, emitting high energy laser pulses at 355, 532 and 1064 nm with a repetition rate of 10 Hz. Its spatial and temporal resolution is 7.5 m and 100 s respectively. The receiving unit, based on a Cassegranian telescope of 300 mm and dichroic mirrors, is able to detect and discriminate the elastic backscattered lidar signals at 355, 532 and 1064 nm and the Raman backscattered ones at 387, 607 and 407 nm. The geometrical specification of EOLE makes feasible the full overlap of the laser beam with the receiver field of view to be reached at heights of the order of 800 m a.g.l. (Kokkalis et al., 2012; Kokkalis, 2017). An additional depolarization channel at 355 nm was added in 2016 in order to obtain the linear particle and volume depolarization ratio vertical profiles in the atmosphere. For its calibration the ± 45° calibration method is implemented (Freudenthaler et al., 2009).

2.2. Granada Raman lidar depolarization system (MULHACEN)

The multiwavelength Raman lidar system MULHACEN (LR331D400 from Raymetrics S.A.), located at the Andalusian Institute for Earth System Research (IISTA-CEAMA) of Granada (37.16° N, 3.61°W, elev. 680 m asl), is configured in a monostatic biaxial alignment pointing vertically to the zenith (Guerrero Rascado et al., 2008, 2009). A pulsed Nd:YAG laser with emission at wavelengths of 355, 532 and 1064 nm is used as a radiation source. The spatial resolution is 7.5 m and the temporal resolution 1 min. The backscattered signals are collected by a Cassegranian telescope and split by dichroic mirrors to detect elastic signals at 355, 532 (in parallel and perpendicular polarizations) and 1064 nm and Raman shifted signals at 387, 607 and 408 nm. Due to the instrument setup, the incomplete overlap limits the lowest possible detection height at 500 m a.g.l. (around 1200 m a.s.l.) (Guerrero-Rascado et al., 2010; Navas-Guzmán et al., 2011). The lidar system was upgraded in 2010 to enable the application of the ± 45° calibration method as presented in Bravo-Aranda et al. (2013).

2.3. CIMEL sun-sky radiometers

The columnar aerosol optical and microphysical properties used in this work are provided by AERONET network (http://aeronet.gsfc.nasa.gov, Holben et al., 1998) which uses Sun/sky photometers (CIMEL). These instruments perform automatic measurements of the direct solar irradiance at wavelengths of 340, 380, 440, 500, 675, 870, 940 and 1020 nm and diffuse sky radiance at 440, 675, 870 and 1020 nm, respectively. The uncertainty of the aerosol size distribution retrieved by the sky radiance measurements is based on the calibration uncertainty of each wavelength, assumed to be < ± 5%. More details can be found in Dubovik and King (2000) and Dubovik et al. (2006).

Due to strict criteria imposed by the AERONET inversion algorithm and the reduced sampling of almucantar sky radiance measurements, there were very few level 2.0 inversion retrievals for both Athens and

Granada. Thus, the AERONET level 1.5 data (cloud screened data with pre- and post-calibrations applied) of Version 3 was used providing information regarding the columnar aerosol optical depth (AOD) at 500 nm, AE and Fine Mode fraction (FMF), the particle volume size distribution (with particle radius range from 0.05 to 15 μm), the single scattering albedo (SSA) and the complex refractive index (CRI). The analysis of these columnar properties for Athens and Granada provides information about how the dust layers affect the atmospheric features at each site.

3. SphInX algorithm

The Spheroidal Inversion eXperiments (SphInX) software tool has been developed at the University of Potsdam (Samaras, 2016) within the Initial Training for atmospheric Remote Sensing (ITaRS) project (2012–2016). This software provides an automated process to carry out microphysical retrievals from synthetic and real lidar data inputs and further to evaluate statistically the inversion outcomes. SphInX software was created to handle non-spherical particles using a two-dimensional (2D) generalization of the Mie model and considering the spheroid-particle approximation. A spheroid is geometrically obtained from a revolution of an ellipse about one of its principle axes. Denoting the semi-minor axis with n and the semi-major axis with b, the aspect ratio ($a = n/b$) can characterize three possible particle shapes: oblate ($a < 1$), sphere ($a = 1$), prolate ($a > 1$). Particle distributions are the main products of the regularized inversion but here depend not only on size (r) but also on shape (α), which is the reason they are referred to as shape-size distributions. There are several common microphysical parameters (redefined to suit the advanced model) and other new shape parameters introduced in SphInX, which can be calculated by knowing the volume shape-size distribution. For this study we will restrict to the following parameters:

The total volume concentration:

$$\mathrm{u_t} = \int_{a_{min}}^{a_{max}} \int_{\mathrm{r_{min}}}^{\mathrm{r_{max}}} \mathrm{u(r,\,a)drd}a \quad [\mu m^3 cm^{-3}] \tag{1}$$

the surface-area concentration

$$\mathrm{a_t} = \int_{a_{min}}^{a_{max}} \int_{\mathrm{r_{min}}}^{\mathrm{r_{max}}} \frac{3}{\pi r^3} G(r,\,a)u(r,\,a)drda \quad [\mu m^3 cm^{-3}] \tag{2}$$

where the function $G(r,a)$ denotes the spheroidal geometrical cross section of the particle, which can be explicitly computed as follows:

$$G(r,\,a) = \begin{cases} 2\pi\left[n^2 + \frac{b^2}{e}\tanh^{-1}(e)\right], & where\ e = \sqrt{1 - b^2/n^2}, \quad if\ a < 1, \\ 4\pi r^2, \quad if\ a = 1, \\ 2\pi\left[n^2 + \frac{nb}{e}\sinh^{-1}(e)\right], & where\ e = \sqrt{1 - n^2/b^2}, \quad if\ a > 1. \end{cases} \tag{3}$$

the effective radius

$$\mathrm{r_{eff}} = 3\,{}^{\mathrm{u_t}}\!/_{\mathrm{a_t}} \quad [\mu m] \tag{4}$$

the effective aspect ratio

$$a_{eff} = \int_{a_{min}}^{a_{max}} \int_{\mathrm{r_{min}}}^{\mathrm{r_{max}}} \mathrm{u(r,\,a)drd}a \Big/ u_t \tag{5}$$

the aspect ratio width

$$a_{width} = \int_{a_{min}}^{a_{max}} (a - a_{eff})^2 \int_{\mathrm{r_{min}}}^{\mathrm{r_{max}}} \mathrm{u(r,\,a)drd}a \Big/ u_t \tag{6}$$

Note that r here plays the role of a radius of a fictitious spherical particle with equal volume to the actual spheroidal one.

The software package consists of three (main) graphical user interfaces (gui), serving different purposes:

- The SphInX Configurator, where all initial calculation parameters for the inversion are set, e.g. size distribution characteristics, lidar setup, mathematical parameter settings (methods, splines, interval partitions and simulation configurations). There is also the possibility of loading netcdf or ascii files with the optical parameters from measurement cases. This gui communicates all initializations to SphInX Main either directly or through user-stored configuration files.
- The SphInX Main, an independent gui where the inversion takes place. This gui is responsible for the resulting microphysical parameters, including visualizations (either real-time or on demand) of the shape-size distribution and the solution space. Owing to the structure of this gui with several mathematical parameters (e.g. regularization parameters), and illustrations of solution spaces, distributions and tabularized retrieval outcomes, here, occur all preliminary tests which are vital for the main runs. This gui communicates all inversion products to SphInX MPP either directly or through user-stored configuration files.
- The SphInX MPP, an independent gui where all microphysical parameters are shown both individually and briefly in tables with an error analysis, regarding accuracy (in case of simulations) and solution uncertainties. This gui focuses mainly on an a posteriori filtering and analysis of the inversion results.

SphInX operates with expendable pre-calculated discretization databases based on spline collocation and on look-up tables of scattering efficiencies using T-matrix theory (Rother and Kahnert, 2009). This is to avoid the computational cost which would otherwise limit the microphysical retrieval to an impractical point. When no information on the linear particle depolarization ratio (δ_{aer}) is given (usual setup "$3\beta_{aer} + 2a_{aer}$"), the software runs using Mie theory. The inversion is done by regularization combined with a parameter choice rule. The following combinations are available:

(i) Truncated singular value decomposition (TSVD) with the discrepancy principle (DP),
(ii) Tikhonov regularization with the L-curve method (LC),
(iii) Padé iteration with the discrepancy principle,
(iv) Tikhonov regularization with the generalized cross validation method (GCV),
(v) Tikhonov regularization with the discrepancy principle, and
(vi) Padé iteration with the L-curve

Details on the widely used methods TSVD and Tikhonov and the parameter choice rules DP, LC and GCV can be found in most books about regularization, for instance Hansen (2010). Padé iteration, in this context, is part of the so-called generalized Runge-Kutta regularization methods (see Böckmann and Kirsche, 2006).

The optical data profiles obtained from hourly averaged vertical profiles of the aerosol optical properties of Raman lidar observations were used as inputs for our inversions. This was done by specifying certain layers of interest and then averaging to produce the 6-point dataset of the so-called $3\beta_{aer} + 2a_{aer} + 1\delta_{aer}$ setup. These thin layers were selected in heights above the atmospheric boundary layer, where the LR and AE values were varying slowly showing homogeneity inside the plumes. The next step was to determine the initial parameters for the retrieval using physical knowledge and/or inversion stability tests.

Such preliminary numerical tests revealed an overall superior behavior of the method Padé-DP as compared to the other built-in methods. This motivated us to choose the Padé iterative regularization method (Böckmann and Kirsche, 2006) for our measurement cases, in particular with a fixed number of 30 iterations. Moreover, a strong tendency to shape-bimodality led us to use 6–8 spline points and the spline degrees 2–4 among the maximum available ranges of 3–20 and 2–6 respectively. The CRI is fed to the software separately for the real and imaginary parts which then constitutes a grid combining the

following default values: Real part (RRI) [1.33, 1.4, 1.5, 1.6, 1.7, 1.8] and Imaginary part (IRI) [0, 0.001, 0.005, 0.01, 0.03, 0.05, 0.1]. Ideally, this grid can be further confined either when there is sufficient knowledge on aerosol composition (or the exact CRI) and/or through numerical tests which indicate unstable or relatively improbable solutions. For our study the CRI grid was narrowed down to (RRI [1.4, 1.5], IRI [0, 0.001, 0.005, 0.01]). Extreme absorption (RRI = 0.05 or 0.03) was ruled out mostly for the following reasons. First, it is expected to manifest itself much less often for dust particles. According to some reports on literature, such values can be found, for instance, directly on dust site (see e.g. Wagner et al., 2012) or when the dust concentration is lower so that a soot-type absorber prevails (see e.g. Schladitz et al., 2009). Therefore, while not improbable we consider those cases much less encountered and not relevant to the presented cases. Second, preliminary runs with higher IRI and/or lower RRI have shown that the resulted shape-size distributions are less easily reconcilable physically, suggesting smoother representations and having undesired systematic behavior. This is indeed an inherent issue of the inversion process since high IRI values and/or low RRI values are known to smooth out the involved scattering cross sections, see e.g. (Samaras, S., 2016; Rother and Kahnert, 2009) and lead to more severely ill-posed problems. Thus, the risk to compromise further the retrieval combined with the relatively small likelihood of high absorption outweighs the benefit here. Higher RRI values impose only a minute variation to the results according to preliminary runs and thus excluded too.

The determination of the CRI grid is known to have a severe impact even for less complicated schemes based on Mie theory and it is apparently applicable here since we add an additional dimension (shape information) and simultaneously we restrict to coarser radius- and aspect ratio ranges. However, massive simulations performed by Samaras (2016) for different atmospheric scenarios showed that microphysical retrievals with an initially known CRI keep high accuracy and small uncertainty levels. Furthermore, variations of the RRI have minor effects in the retrieved parameters a_t, v_t, r_{eff} and variations of the IRI adds a relatively conservative percentage of 3–20% to the uncertainties compared to the fixed-RI retrievals when the imposed measurement error is reasonably contained. For the retrieval of the shape parameters, the situation is more complicated, and simulations suggest that the quality of the results depend additionally on particle size. Detailed implications of possible variations in shape (α), size (r), and composition (CRI) in the context of simulations exceed the scope of this article and will be revisited exclusively in a future study as a subject of great theoretical interest.

For the shape-size distribution we used a grid of 30×30 (r× a) points with the radius $r \in [0.01, 2.2]$ in μm and the aspect ratio $a \in [0.67, 1.5]$. While both ranges are the maximum available in the software using the spheroid-particle approximation, there is no such (radius) restriction for runs in "spherical" (Mie) mode in the software. Having specified the initial parameters, the inversion is ready to take place and produce the volume shape-size distribution, the refractive index and the parameters (1–6).

All methods in SphInX share a common algorithm primarily aiming to extract the unknown volume shape-size distribution and calculate the rest of the parameters (except CRI) in a second step. First the solution space has to be determined in terms of a specific spline point number and degree which is normally a part of the aforementioned initial parameters. Instead, we only define loosely a range for these parameters and run the inversion for every spline point number and degree within this range and for every CRI. Then we make forward calculations for all solutions, and pick the one CRI associated with the solution with the least residual error. We repeat the process for all spline point numbers and degrees and order the solutions in decreasing quality order (residual-error-wise). Finally, we calculate the mean solution (distribution and CRI) out of the first few least-residual solutions and then the rest microphysical products using the equations (1)–(6). We will refer to the selected solutions and the corresponding parameters as the "best". This approach is based on hybrid regularization methods described in detail in (Samaras et al., 2015; Samaras, 2016).

This algorithm allows for a straightforward uncertainty calculation. The Variability (Var %) of a parameter here stands for the standard deviation of the selected best (least-residual) values, divided by their mean value. If there are multiple datasets, then a mean variability is implied, i.e. Var is found for each dataset and then their mean value is assigned to Var. Moreover, in the latter case, the Uncertainty *(Unc %)* of a parameter is the ratio of the standard deviation of the mean values of this parameter for each dataset over their mean. For simulations, the different datasets are usually produced with random realizations of input error added to a synthetic dataset, and therefore Unc is a measure of numerical stability. For measurement cases, these datasets could consist of optical data values related to consecutive smaller "sub-layers" of a layer which is partitioned in order to keep intensive parameters (e.g. AE, LR) relatively constant, and therefore Unc serves as an additional measure of variability among the retrieved solutions.

4. Air mass analysis

To verify that the source region of the air masses arriving over Athens and Granada, is originating over the African continent, an analysis of backward trajectories was performed by means of the HYSPLIT model (Hybrid Single-Particle Lagrangian Integrated Trajectory, Stein et al., 2015; Rolph et al., 2017). All trajectories were calculated for a period of 120 h backward in time and were computed for arrival heights of approximately the bottom, center and top of the observed layers. In this study, transport time refers to the time that the air masses travelled after leaving the African continent and until they were detected over our stations. Based on this transport time, the four selected dust cases reveal a pattern which allows us to separate them into two categories: (i) transport time ≤ 1 day, which indicates quite pure or less mixed particles within the dust layer (Fig. 1), (ii) transport time > 1 day, which indicates a combination of mineral dust, polluted mineral dust or even smoke arriving over the stations (Fig. 2).

i) **Transport time (after African continent) ≤ 1 day:** The air mass backward trajectories arriving over Athens on 11 September 2017 (case A), at 18:00 UTC, between 2 and 4 km (cf. Fig. 1 left), shows that ~18 h of the total of 120 h of the residence time are spent over the Mediterranean Sea and 60 (at 3000 m) to 100 h (at 4000 m) over S. Morocco, Algeria and Libya, where Saharan desert areas spread out. Similarly, for the air mass backward trajectories arriving over Granada on 16 June 2013 (case B), at 22:00 UTC, between 2.5 and 4 km, (cf. Fig. 1 right), ~24 h are spent over N. Morocco and Alboran Sea and 48 h (at 2500 and 3000 m) over E. Morocco and Algeria, areas that belong to the Saharan region. Consequently, the aforementioned air masses in both cases are travelling quite fast (≤ 1day), probably favoring the direct transport of mineral dust aerosols.

ii) **Transport time (after African continent) > 1 day:** For the case of 19 April 2018 detected over Athens (case C), the air mass backward trajectories calculated at 18:00 UTC, show that less than 30 of the total 120 h are spent over Libya and Tunisia while the rest 90 h are spent circulating over Mediterranean, Aegean Sea and Bulgaria (cf. Fig. 2 left). Analogously, for the case of 9 June 2016 detected over Granada (case D), the calculated backward trajectories at 02:00 UTC, show that ~48 of the total 120 h are spent over the Atlantic Ocean and the Andalusian region while the other 72 h over S. Morocco and Algeria (cf. Fig. 2 right). It is evident that in both those events, there is no direct air mass flow from the source region to the lidar stations, but an alternative path above marine and urban areas. Therefore, the measured aerosol optical properties for these cases can be attributed to a mixing state where industrial, marine or even biomass burning aerosols were possibly mixed with the desert dust

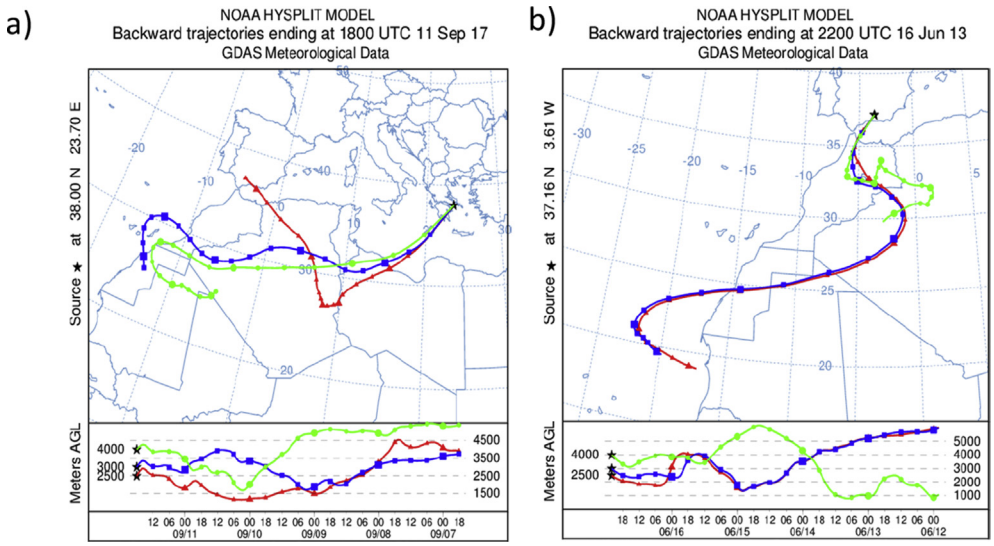

Fig. 1. 120-h air mass backward trajectories arriving over a) Athens on 11/09/2017, (case A, 18:00 UTC), between 2 and 4 km height and b) Granada on 16/06/2013, (case B, 22:00 UTC), between 2.5 and 4 km height.

aerosols.

In order to investigate the possible mixing with other aerosol particle types during the air masses transport, we used the observations of the spaceborne CALIOP (Cloud-Aerosol Lidar with Orthogonal Polarization) to track the aerosol plumes for the cases of the second category. This lidar system is onboard the CALIPSO (Cloud-Aerosol Lidar and Infrared Pathfinder Satellite Observation) mission. In this work we used the aerosol typing product of (Kim et al., 2018). We found CALIPSO overpasses that were intersecting the backward trajectories as presented in Fig. 2 (red boxes). Using the aerosol typing mask, it was possible to determine the degree of mixing for these two cases. It is easily observed that the air masses that eventually arrived over Athens at 19 April 2018 contained not only pure mineral dust, but also polluted dust and even some smoke particles (yellow, brown and black colors respectively). Moreover, the case of 9 June 2016 shows that mainly pure dust (above 3 km) and polluted dust (below 3 km) was transported over Granada. Keeping this information in mind, we could expect different features in terms of optical and microphysical properties for these two dust transport cases. It should be mentioned here that there were no CALIPSO data available for case A and no overpass over Spain for case B, consequently no such info is given for Fig. 1a and b.

5. Particle optical and microphysical characterization

In this section, the presented results pertain to i) columnar properties from AERONET retrievals, ii) vertical profiles of the aerosol optical properties from lidar data using Raman inversion algorithms and iii) microphysical properties from Raman lidar using the SphInX software. Since the AERONET derived aerosol size distributions refer to columnar values with aerosol radius ranging from 0.01 μm up to 15 μm and were performed earlier than the nighttime lidar measurements, no direct comparison with SphInX results is implemented. However, the coherence of results can be shown.

5.1. Column-integrated aerosol properties

The main direct AERONET products obtained for the relevant selected temporal windows are summarized in Table 1. The AOD at 500 nm was at least 0.27, with relatively low FMF values in all cases but C. In this case, the presence of polluted and smoke particles (see section 3) makes the fine and coarse mode (related to mineral dust) share

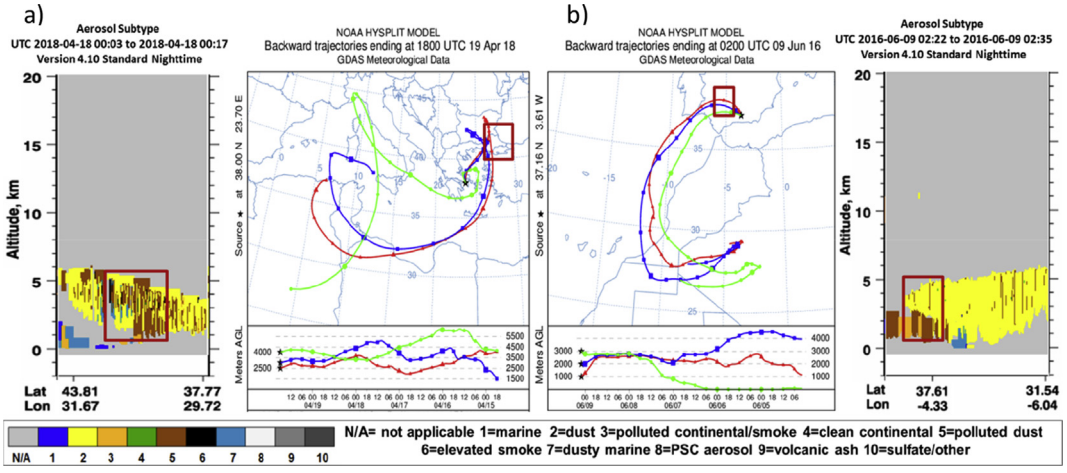

Fig. 2. 120-h backward trajectories over a) Athens on 19/04/2018, (case C, 18:00 UTC), between 2.5 and 4.5 km and b) Granada on 09/06/2016, (case D, 02:00 UTC), between 1 and 3 km height, along with position (altitude, latitude and longitude) and type of the aerosol layers detected by CALIOP during one overpass tracking the air masses contained within the red boxes (extreme left and right). Yellow and brown colors stand for pure and polluted dust respectively, while black indicates smoke. (For interpretation of the references to color in this figure legend, the reader is referred to the Web version of this article.)

Table 1
Columnar properties retrieved from direct AEORNET measurements.

Case	Time (UTC)	AOD (500 nm)	FMF (%)	AE_{AOD} (440/870 nm)
A) AT, 11/09/2017	15:36	0.34	22	0.22
B) GR, 16/06/2013	18:28	0.27	28	0.36
C) AT, 19/04/2018	15:20	0.27	55	0.94
D) GR, 09/06/2016	18:21	0.54	19	0.16

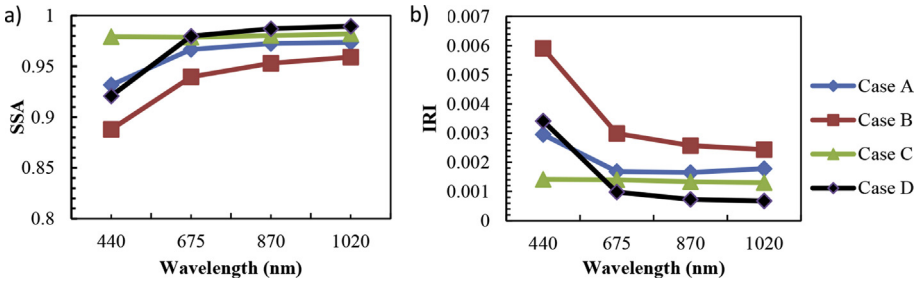

Fig. 3. AERONET retrievals of a) SSA and b) IRI for cases A to D.

similar proportions with a FMF of 55%. The spectral dependent AOD's and AE_{AOD}'s show values much lower than the usual for urban sites (e.g. Alados-Arboledas et al., 2003, 2008; Lyamani et al., 2010; Gerasopoulos et al., 2011), again with the exception of case C, where AE value is close to 1, a representative value for mixed biomass burning with desert dust aerosols (Giannakaki et al., 2016).

In order to characterize the aerosol particles in the atmospheric column in more detail, selected products provided by AERONET inversions (using AOD and sky radiance measurements) were analyzed. In Fig. 3 (left), we can observe typical SSA values for dust particles increasing with wavelength, except case C, ranging from 0.85 to 0.98 as also observed by Dubovik et al. (2002), Valenzuela et al. (2012) and Benavent-Oltra et al. (2017). The IRI values (Fig. 3 right), especially in case B, are a bit higher than the reported by Dubovik et al. (2002), but agree with those from Benavent-Oltra et al. (2017). The spectral behavior of these two variables (SSA, IRI) yields further interesting information. The cases with shorter transport time (case A and B) have similar positive slope for SSA and negative for IRI, as also reported in the literature (Toledano et al., 2011; Valenzuela et al., 2012; Lopatin et al., 2013; Schuster et al., 2016; Benavent-Oltra et al., 2017). For case C, where the dust was transported during longer time and there is a strong possibility of mixing with biomass burning particles, we can observe no dependence on wavelength (zero slope), a feature related to the presence of black carbon from combustion (Bergstrom et al., 2007). In case D, where again the transport process last longer, the spectral dependence is more pronounced in the shorter wavelengths showing similarities with cases A and B. These results suggest that the higher the element of dust and the contribution of larger particles in the mixing, the more pronounced spectral difference for smaller wavelengths. Moreover, absorption is lower and SSA is higher in general for the cases with more aged or mixed particles (cases C and D). It should be noted here that there have been numerous studies providing fundamental insights into the complex photochemistry of mineral dust aerosol in the atmosphere (Cwiertny et al., 2008). Liquid or adsorbed water and coatings can affect dust photochemistry as mineral dust particles are transported through the atmosphere, as well as the diurnal cycle can affect the mineral dust properties between daytime (AERONET) and nighttime (Raman-lidar) measurements.

In all four studied cases, the size distributions retrieved by AERONET inversion code, showed again that the fine modes are not significant compared to the coarse modes that are dominant in the atmospheric column (Fig. 4). This means a contribution of larger particles that corroborates the desert origin of the aerosols. The dominance of coarse mode particles is highlighted by the bimodal size distribution

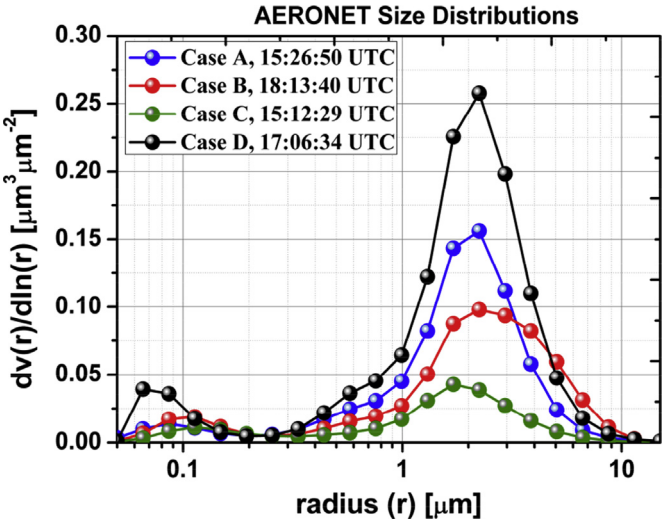

Fig. 4. AERONET volume size distributions dV(r)/dln(r) for cases A to D.

with separation radius ranging from 0.18 μm to 0.30 μm. For our first category (Cases A and B), the bi-modal volume size distributions have almost similar structure with low fine mode concentration (< 0.02 $\mu m^3/\mu m^2$). Specifically, for case B, the coarse mode is shifted to a bit larger radii while a small difference in maximum volume concentration equal to 0.06 $\mu m^3/\mu m^2$ indicates quite similar intensity of the events of cases A and B. For our second category (Cases C and D), a large difference in the size distributions between the two events is obvious. A high peak of coarse mode for case D in comparison to the lower concentration of case C represents a more intense dust episode. The highest intensity differences among the dust episodes are mostly reflected by the associated magnitudes of the volume concentration. For instance, the highest coarse-mode peak, corresponding to Case D, represents a relatively more intense dust episode as compared e.g. to the lowest peak corresponding to case C. There are further differences to be observed regarding the shape of the coarse mode with the most evident one corresponding to the mode width, which is substantially greater for case D than for case C having ranges 0.33–8.65 μm and 0.44–6.64 μm respectively.

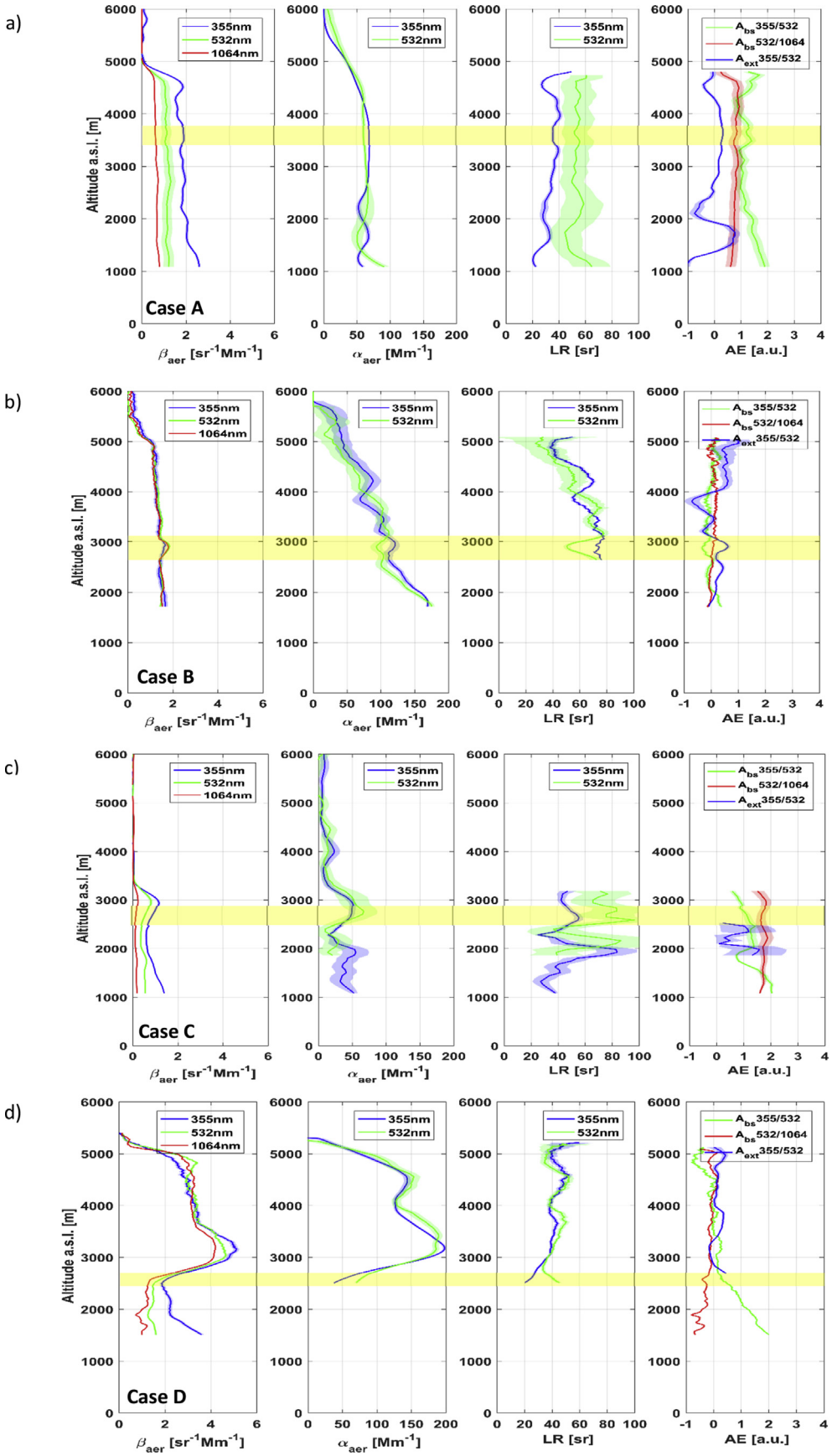

Fig. 5. Vertical profiles of the aerosol optical properties (βaer, α_{aer}, LR, AE) obtained over a) Athens on 11 September 2017, 17:00–18:30 UTC (Case A), b) Granada on 16 June 2013, 22:00–22:30 UTC (Case B), c) Athens on 19 April 2018, 17:30–18:50 UTC (case C), between and d) Granada on 9 June 2016, 01:00–02:00 UTC (case D) along with their error estimations (horizontal bounds). Yellow layers indicate the regions selected for microphysical analysis. (For interpretation of the references to color in this figure legend, the reader is referred to the Web version of this article.)

5.2. Vertically-resolved aerosol properties

5.2.1. Optical properties

Fig. 5 (a and b) depicts the vertical profiles of the dust aerosol optical properties of the two independent mineral dust cases A and B. On 11 September 2017 (Fig. 5a) a thick, intense and almost uniform dust layer from around ground level up to 4.5 km height (a.s.l.) was detected by EOLE [17:00–18:30 UTC] over Athens. On 16 June 2013 (Fig. 5b) there is an almost uniform layer in the atmospheric column above Granada, which, similarly to case A is reaching 4.7 km above ground level [22:00–22:30 UTC]. For the aforementioned cases we selected the thin layers 3.5–3.8 and 2.65–3.1 km a.s.l. respectively. The selection of these thin layers inside the dust plumes was based not only on the homogeneity of the optical properties, but also on the backward trajectories in which, at roughly these altitudes, the source region is the same (W. Algeria) as shown in Fig. 1. The vertical profiles of the other two cases representing events of more aged and mixed dust layers are also presented in Fig. 5 (c and d). At least two decoupled aerosol layers of different intensities are detected over Athens on 19 April 2018 (Fig. 5c) between 1.5 and 4.5 km a.s.l. [17:30–18:50 UTC]. The vertical profiles on 9 June 2016 in Granada (Fig. 5d) confirm the decoupled thick mineral dust layer of different intensities, between 2.5 and 5 km a.s.l. Here, we selected the thin layers 2.6–2.8 [17:30–18:50 UTC] and 2.55–2.75 km a.s.l. [01:00–02:00 UTC] respectively in which there was indication of mixed layers; polluted dust or even smoke particles for case C, polluted dust for case D (see also Fig. 2).

Within all four selected aerosol layers of our independent cases studied here, the mean values of the optical properties obtained from the lidar measurements and used for the inversions are shown in Table 2, along with their standard deviation. Their intensive parameters are also presented. For the first two cases (A and B) with transport time less than one day these values represent the typical optical properties of short range transported dust plumes. More specifically, typical LRs were found (54 ± 1 and 64 ± 6 sr at 532 nm respectively) falling within the ranges for Saharan-dust particles found in literature (Müller et al., 2009; Groβ et al., 2011). The backscatter related AE ($AE_{b532/1064}$) values of 0.83 ± 0.04 and 0.03 ± 0.02 respectively correspond to quite large particles in accordance with previous findings (Mamouri and Ansmann, 2014; Veselovskii et al., 2016). The small standard deviation values underline that aerosol particles were well mixed in the altitude range of the uniform dust layers. Concerning the remaining two cases (C and D) we found larger deviations among their intensive optical properties. Quite high mean LR value of 79 ± 5 sr (at 532 nm) for case C corroborate the strong indication that dust particles were mixed with particles of other origins such as smoke while travelling. Lower LR values of 39 ± 2 sr (at 532 nm) for case D. Contrary to the category with transport time up to one day, here, the decoupled plumes were probably relatively inhomogeneously distributed along the vertical direction and mixed with aerosols from different origins (possible biomass burning mixtures for case C and polluted mixtures for case D) or even different regions in Sahara desert (differences in chemical composition of the mineral dust).

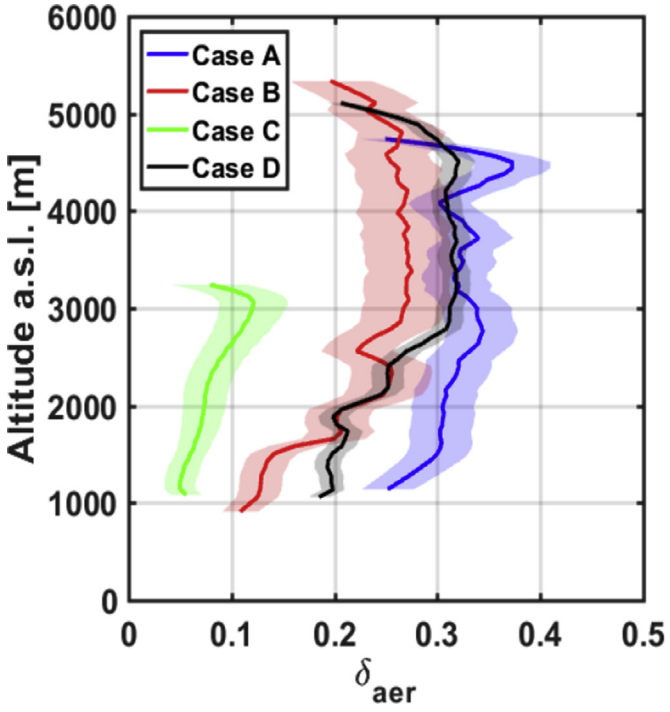

Fig. 6. Vertical profiles of the δ_{aer} for cases A to D along with their error estimations (horizontal bounds). For Athens and Granada stations depolarization measurements are available at 355 nm and at 532 nm respectively.

Fig. 6 presents the vertical profiles of δ_{aer} of the four case studies (at 355 nm for Athens and at 532 nm for Granada system). Typical values of desert dust δ_{aer} (Freudenthaler et al., 2009; Groβ et al., 2015), were calculated for the cases of the first category, verifying again the dominance of the mineral particles. More specifically, mean δ_{aer} values equal to 0.34 ± 0.02 for case A (17:30–18:30 UTC, 3.5–3.8 km) and 0.26 ± 0.04 for case B (22:00–22:30 UTC, 2.65–3.10 km)) provide a clear indication of the non-sphericity of the pure dust particles. For these cases, the particles of mineral dust sources seem to be rather unaffected by anthropogenic or other polluted aerosols. For the cases of the second category, the mean δ_{aer} calculated inside the plumes show marginal standard deviation. The value of δ_{aer} was found equal to 0.11 ± 0.01 for case C (17:30–18:30 UTC, 2.6–2.8 km) and 0.28 ± 0.01 for case D (01:00–02:00 UTC, 2.55–2.75 km). The fact that in case D the value of δ_{aer} increases above 2.5 km a.s.l. (δ_{aer} = 0.32 ± 0.01, 3–4.5 km) confirms the separation between polluted and pure dust layers observed by CALIPSO (see Fig. 2b). Moreover, the aforementioned influence of mixtures (dust and smoke) can explain the lower δ_{aer} values of around 10% calculated for case C, which are in accordance with previous studies (Ansmann et al., 2011; Groβ et al., 2011; Tesche et al., 2011;

Table 2
Average particle optical properties for the selected thin layers within the dust zone along with their standard deviation.

Case		A	B	C	D
Layer height a.s.l. [km]		3.50–3.80	2.65–3.10	2.60–2.80	2.55–2.75
Optical properties	**α355 [Mm^{-1}]**	68.62 ± 0.89	115.60 ± 6.94	49.11 ± 3.13	62.27 ± 1.62
	β355 [Mm^{-1} sr^{-1}]	1.89 ± 0.06	1.55 ± 0.11	0.94 ± 0.11	2.39 ± 0.43
	α532 [Mm^{-1}]	60.69 ± 0.52	100.88 ± 8.35	52.54 ± 9.00	82.67 ± 10.06
	β532 [Mm^{-1} sr^{-1}]	1.13 ± 0.03	1.67 ± 0.06	0.61 ± 0.10	2.15 ± 0.05
	β1064 [Mm^{-1} sr^{-1}]	0.63 ± 0.01	1.621 ± 0.001	0.18 ± 0.02	1.83 ± 0.05
	δ_{aer} 355, 532	0.34 ± 0.02	0.26 ± 0.04	0.11 ± 0.01	0.28 ± 0.01
Intensive properties	**LR355 [sr]**	36 ± 1	76 ± 7	51 ± 4	28 ± 4
	LR532 [sr]	54 ± 1	64 ± 6	79 ± 5	39 ± 2
	Ae_{β} 532/1064	0.83 ± 0.04	0.03 ± 0.02	1.70 ± 0.20	0.25 ± 0.10

Table 3
Average particle microphysical properties for the selected thin layers along with their Var (%) (see Section 2), based on the 5 best solutions picked by the software.

Case		A	B	C	D
Layer height a.s.l. [km]		3.50–3.80	2.65–3.10	2.60–2.80	2.55–2.75
Lidar-based inversions	a_t [$\mu m^2 cm^{-3}$]	152.20 ± 8%	268.30 ± 10%	140.99 ± 3%	228.73 ± 5%
	u_t [$\mu m^3 cm^{-3}$]	16.13 ± 10%	29.42 ± 13%	19.92 ± 8%	36.64 ± 6%
	r_{eff} [μm]	0.32 ± 4%	0.33 ± 3%	0.42 ± 8%	0.48 ± 8%
	α_{eff}	1.18 ± 5%	1.14 ± 5%	1.32 ± 1%	1.32 ± 1%
	α_{width}	0.06 ± 24%	0.06 ± 25%	0.06 ± 15%	0.06 ± 25%
	Distribution uncertainty [%]	48.19	46.31	26.86	23.85
Microphysical properties	RRI	1.4 ± 0%	1.4 ± 0%	1.5 ± 0%	1.5 ± 0%
	IRI	0.004 ± 43%	0.004 ± 57%	0.002 ± 50%	0.005 ± 42%
	SSA [532 nm]	0.97 ± 1%	0.98 ± 2%	0.98 ± 2%	0.96 ± 2%

Wandinger et al., 2016; Giannakaki et al., 2016).

5.2.2. Microphysical properties

For each selected dust layer, the SphInX inversion algorithm was applied using the mean values of our optical datasets analyzed in Table 2 as inputs. Table 3 shows the average values of a_t, u_t, r_{eff}, a_{eff} and α_{width}, RRI, IRI and SSA, along with their Var (%) derived by using the 5 best solutions picked by the software according to the algorithm described previously.

The RI for the mineral dust cases of the first category is found equal to 1.4 + 0.004i inside both selected layers and SSA (532 nm) equal to 0.97 for case A and 0.98 for case B, which points to weakly absorbing particles. On the other hand, different values of the CRIs were found for the cases of the second category. More specifically, for case C the CRI was found equal to 1.5 + 0.002i while for case D it was found equal to 1.5 + 0.005i.

For the less mixed dust episodes the retrieved 2D shape-size distributions reveal the same three-mode pattern (Fig. 7 a and b). Two of the three modes correspond to prolate particles ($a \approx 1.5$), confirming the non-spherical nature of the dust particles. The prolate particle modes can be subdivided into a coarse mode with radii $r \approx 1.7$ μm and a fine mode around 0.5 μm. A third mode centered in $a \approx 1$ and $r \approx 0.3$ μm represents an additional contribution of spherical particles. The effective radius for the more intense episode of case A is found shifted to larger values (0.57 ± 0.05 μm) as compared to the corresponding case B (0.33 ± 0.02 μm).

In Fig. 7c, the dominant mode of the shape-size distribution corresponds to prolate fine particles (up to $\alpha \approx 1.5$, $r \approx 0.5$ μm) and is extended up to 2.2 μm. There is a less prominent but substantially wider mode pertaining to prolate coarse particles (up to $\alpha \approx 1.5$, $r \approx 1.4$ μm) with a less obvious separation point. Furthermore, the smaller peak indicates a contribution of oblate fine particles ($\alpha \approx 0.7$, $r \approx 0.3$ μm). However, due to the relatively low magnitude of this peak and the possibility of oversmoothing of the prolate coarse mode, the case that this peak might be either a suppressed larger peak or an artifact, should be considered as well. In Fig. 7d, the dominant mode of the shape-size distribution has similar behavior with the one of case C concerning the prolate fine mode (up to $\alpha \approx 1.5$, $r \approx 0.5$ μm, extended up to 2.2 μm). However, the less prominent mode pertaining again to prolate coarse particles seems to be extended to smaller α values ($\alpha \approx 1.3$, $r \approx 1.5$ μm). Here, there is a more significant coarse mode contribution in accordance with the higher δ_{aer} value compared to case C. For these four cases the dust particles behave effectively as prolate spheroids as it is further indicated by the values of α_{eff} ranging between 1.19 − 1.32 (see Table 3). The value of a_{width} was calculated equal to 0.06 ± 0.01 for all cases. The differences in the shape size distributions for the cases presented in Fig. 7 provide an additional indication for differences in aerosol composition occurring due to the different travelled path bound to each case. Since case D owns the most intensive event (see Fig. 5) it takes the greatest u_t value equal to 37 $\mu m^3 cm^{-3}$, while for the rest cases A, B and C we have 16, 29, and 20 $\mu m^3 cm^{-3}$ respectively (see Table 3).

Restricting to a one-dimensional size distribution would offer a short-sighted view. If we picture, for instance, all aspect ratio contributions summed for the distributions in Fig. 7(a and b,c,d) so that there is only radius dependence left, then the figures would appear relatively similar in trend qualitatively. Obviously, even the spheroidal consideration of dust particles does not capture the particle form physically (it is mainly a better fit for the observed optical properties), but with the described approach our analysis can be refined to include possible diversity among cases of interest which is otherwise invisible.

Although these 2D particle distributions provide more information than a usual size distribution there are also limitations to this approach which might affect the inversion outcome. Since there are several assumptions pertaining to the whole inversion chain (discretization, regularization, T-matrix theory etc.), a full discussion exceeds the scope of this article and will limit itself to some evident remarks. The less pronounced separation between fine and coarse modes especially for the prolate part in Fig. 7 might indicate higher measurement errors which were misidentified by regularization; this is a common encounter also for the usual one-dimensional (size) distributions, (see Samaras et al., 2015). The higher aspect ratio end (1.5) might not be sufficient in order to reveal the full extent of the shape size distribution further along the aspect ratio axis. The same is true for the radius boundary on the right end even though in our cases the distributions are only mildly abrupt in this respect. Finally, the presence of potential small artifacts in the distribution, like for instance in Fig. 7 (c and d) has only small contribution to the derived microphysical parameters since the double integration suppresses further small oscillations in the solution.

The results obtained in this study (Tables 2 and 3) can be compared with other values found in the literature about transported Saharan dust events detected over Europe, Morocco and Cape Verde as summarized in Table 4.

6. Summary

During strong Saharan dust events that occurred over Athens and Granada, selected lidar measurements were performed to retrieve the optical properties of dust particles in the lower free troposphere. The cases were separated into two categories based on their transport duration time focusing on short range (pure) to long range (mixture) dust processes. This categorization was based mainly on the air mass back-trajectories from HYSPLIT model that were pointing to the Saharan desert. CALIPSO data provided further information about the aerosol typing. The SphInX software tool was used to derive the mean microphysical properties of dust particles for the four independent dust events selected here running with $3\beta_{aer} + 2a_{aer} + 1\delta_{aer}$ input datasets. Padé method with fixed iteration equal to 30 was chosen for the inversion among the other available methods in SphInX on the basis of preliminary runs which favored its suitability.

Similarities were found between the cases A and B of the first category (transport time ≤ 1 day with origin W. Algeria) concerning the optical properties (LR 54 ± 1 sr and 64 ± 6 sr at 532 nm respectively),

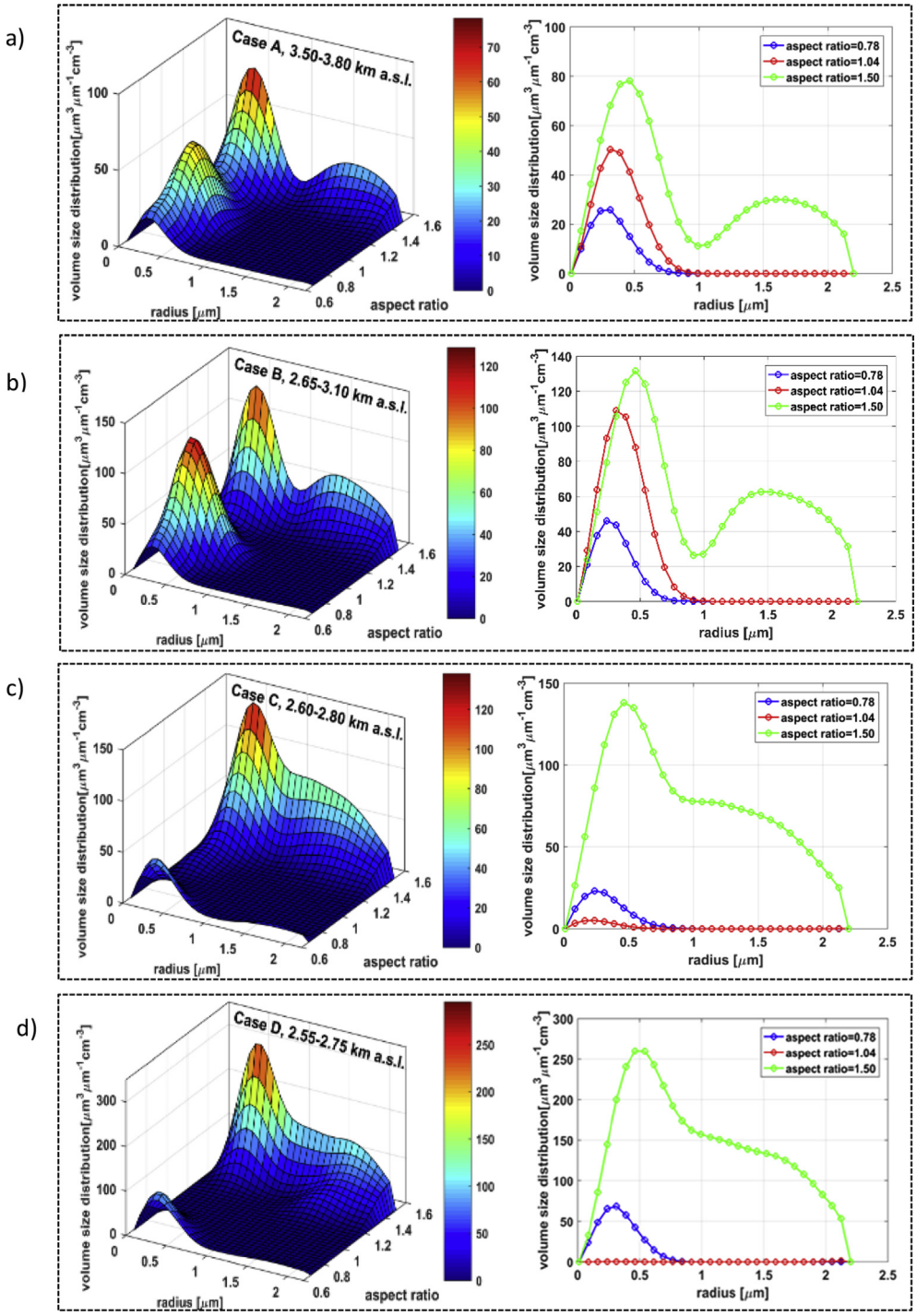

Fig. 7. The shape-size distribution shown in 3D (left) for the hole aspect ratio range and in 2D (right) for 3selected aspect ratio values (0.78-oblate, 1.04-spherical, 1.50-prolate particles) for a) ca se A at 3.5–3.8 km a.s.l., b) case B at 2.65–3.10 km a.s.l., c) case C at 2.6–2.8 km a.s.l. and d) case D at 2.55–2.75 km a.s.l. as retrieved by SphInX software tool.

the shape size distribution, the RI values ($1.4 + 0.004i$ in both dust cases) and the aspect ratio ($a_{eff} = 1.19$ and $a_{width} = 0.06$). On the contrary, there are differences in the aforementioned parameters among the two categories. The LR values are higher for the more mixed case C and lower for the long range transported case D (79 ± 5 sr and 39 ± 2 sr, at 532 nm respectively). The mean $AE_{b532/1064}$ ranges within 0.03–0.83 for the less mixed cases indicating quite large particles, while it is equal to 1.7 for polluted dust mixed with smoke. Moreover, the mean δ_{aer} ranges from 11 to 34%, for the cases A, B and C, D depending on the aerosol composition. This variability is expected not only because of the different Saharan region but also because of the different path travelled (Balkans for case C and over Atlantic for case D) which further translates to different aging and mixing processes. The retrieved RI values were found equal to $1.5 + 0.002i$ for case C and $1.5 + 0.005i$ for case D, while a_{eff} values around 1.32 for both cases pertaining to volume size distributions mainly with prolate particles.

Selected column-integrated aerosol properties were also presented for a comprehensive analysis. High AOD values (at 500 nm) were shown ranging from 0.27 to 0.54, depending on the intensity of each event, while the calculated FMF (19–55%) and the spectral dependence

Table 4
Optical and microphysical properties found in the literature about transported Saharan dust events detected in Europe, Morocco and Cape Verde used to compare with the obtained values in Tables 2 and 3

Reference	Region	Technique	Type	LR (λ)	β-AE (λ)	α-AE (λ)	δp (λ)	RRI (λ)	IRI (λ)	SSA (λ)	r_{eff}
Mattis et al. (2002b)	Leipzig (51.3° N, 12.4° E)	Lidar	Dust	60–100 sr (355 nm) 50–80 sr (532 nm)			0.15–0.25 (532 nm)				
Papayannis et al. (2005)	Athens (37.9° N, 23.8° E)	Lidar	Dust	53 ± 1 sr (355 nm)							
Guerrero-Rascado et al. (2008)	Granada (37.16° N, 3.61° W)	Lidar	Dust	41–45 sr (532 nm)			0.15–0.25 (532 nm)				
Guerrero-Rascado et al. (2009a)	Granada (37.16° N, 3.61° W)	Lidar	Dust	50–65 sr (532 nm)	−0.4–0.5 (355/532 nm)						
Freudenthaler et al. (2009b)	Quarzazate, Morocco (30.94° N, 6.91° W)	Lidar	Pure dust				0.26 ± 0.06 (355 nm) 0.30 ± 0.00 (532 nm) 0.28 ± 0.05 (710 nm) 0.27 ± 0.04 (1064 nm)				
Petzold et al. (2009)	S Morocco (30.93° N, 6.91° W)	In Situ	Dust					1.550–1.565 (450 nm) 1.549–1.561 (550 nm) 1.546–1.555 (700 nm)	0.0031–0.0052 (450 nm) 0.0016–0.0042 (550 nm) 0.0003–0.0025 (700 nm)		
Córdoba-Jabonero et al. (2011)	Santa Cruz de Tenerife (28.5° N, 16.2° W); El Arenosillo (37.1°N, 6.7° W); Granada (37.16° N, 3.61° W)	Lidar and In situ	Pure dust	45–70 sr (532 nm)							0.10–0.15 μm (fine) 1.06–1.72 μm (coarse)
Bauer et al. (2011)	Praia, Cape Verde (14.95° N, 23.49° W)	In Situ	Pure dust							0.92 ± 0.07 (532 nm)	
Groβ et al. (2011b)	Praia, Cape Verde (14.95° N, 23.49° E)	Lidar	Dust	58 ± 7 sr (355 nm) 62 ± 5 sr (532 nm)			0.25 ± 0.03 (355 nm) 0.30 ± 0.01 (532 nm)				
Tesche et al. (2011)	Praia, Cape Verde (14.95° N, 23.49° E)	Lidar	Dust	53 ± 10 sr (355, 532 nm)	0.2 ± 0.3 (355/532 nm) 0.45 ± 0.16 (532/1064 nm)	0.2 ± 0.3 (355/532 nm)	0.31–0.10 (532 nm) 0.37 ± 0.07 (710 nm)				
Tesche et al. (2011)	Praia, Cape Verde (14.95° N, 23.49° E)	Lidar	Dust/smoke	67 ± 14 sr (355, 532 nm)	0.7 ± 0.3 (355/532 nm, 532/1064 nm)	0.7 ± 0.4 (355/532 nm)	0.15–0.05 (532 nm) 0.2 ± 0.1 (710 nm)				
Weinzierl et al. (2011)	Praia, Cape Verde (14.95° N, 23.49° E)	In situ	Dust					1.550 ± 0.002 (467 nm) 1.550 ± 0.002 (530 nm) 1.546 ± 0.002 (660 nm)	0.004 ± 0.002 (467 nm) 0.003 ± 0.002 (530 nm) 0.001 ± 0.001 (660 nm)		1.21 ± 0.32 μm
Weinzierl et al. (2011)	Praia, Cape Verde (14.95° N, 23.49° E)	Lidar Photometry	Dust	42 ± 5 sr (532 nm)			0.22 ± 0.04				

(*continued on next page*)

Table 4 (*continued*)

Reference	Region	Technique	Type	LR (λ)	β-AE (λ)	α-AE (λ)	δp (λ)	RRI (λ)	IRI (λ)	SSA (λ)	r_{eff}
Toledano et al. (2011)	Praia, Cape Verde (14.95° N, 23.49° E)									0.93 ± 0.01 (440 nm) 0.98–0.99 (670, 1020 nm)	
Preißler et al. (2011)	Évora (38.57° N, 7.91° W)	Lidar	Dust	45 ± 11 sr (355 nm) 53 ± 7 (532 nm)	0.4 ± 0.6 (355/532 nm) 0.4 ± 0.2 (532/1064 nm)	0.0 ± 0.2 (355/532 nm)	0.28 ± 0.04 (532 nm)				
Valenzuela et al. (2014)	Alborán Island (35.95° N, 3.03° W)	Photometry								0.88 ± 0.03 (440 nm) 0.91 ± 0.03 (1020 nm)	
Bravo-Aranda et al. (2015)	Granada (37.16° N, 3.61° W)	Lidar	Dust		0.8 ± 0.1 (355/532 nm)		0.19 ± 0.03 (532 nm)				
Denjean et al. (2016)	Western Mediterranean Basin	Airborne In situ	Dust					1.50–1.55 (530 nm)	0.000–0.005 (530 nm)	0.90–1.00 (530 nm)	
Benavent-Oltra et al. (2017b)	Granada (37.16° N, 3.61° W)	Lidar and Photometry	Dust		0.5 ± 0.2 (532/1064 nm)			1.52–1.55 [355, 1064 nm]	0.001–0.013 (355 nm) 0.002–0.004 (640 nm) 0.001–0.003 (1064 nm)	0.86–0.95 (355 nm) 0.90–0.96 (640 nm) 0.96–0.99 (1064 nm)	0.10–0.13 μm (fine) 2.2–2.4 μm (coarse)

of SSA and IRI revealed the impact of the different aerosol types in terms of mixing.

In spite of the apparent limitations (restricted aspect ratio/radius domain) of this approach it was demonstrated that the microphysical problem for non-spherical particles can be successfully addressed. Moreover, the 2D volume distributions offer a new and more informative take on the characterization of aerosols with respect to size and shape which further provides insight for the particle mixing in this respect. Additional studies based on multi-wavelength lidar data using SphInX software tool are suggested to be performed so as to improve our knowledge on the aging and mixing aerosol processes and to enrich the aerosol microphysical properties database over Southern Europe.

Declaration of interests

The authors declare that they have no known competing financial interests or personal relationships that could have appeared to influence the work reported in this paper.

The authors declare the following financial interests/personal relationships which may be considered as potential competing interests:

Acknowledgments

O. S.'s research project has been financed through a scholarship from the General Secretariat for Research and Technology (GSRT) and the Hellenic Foundation for Research and Innovation (HFRI). The co-authors from the University of Granada were mainly supported by the Spanish Ministry of Sciences, Innovation and Universities through project CGL2016-81092, by the Spanish Ministry of Education, Culture and Sports through grant FPU14/03684 and by the University of Granada through the contract "Plan Propio. Programa 9. Convocatoria 2013". The financial support for EARLINET in the ACTRIS Research Infrastructure Project by the European Union's Horizon 2020 research and innovation program under grant agreement no. 654169 is gratefully acknowledged. O.S. and P. O-A. were further supported by the Erasmus+ programme of the European Union. The authors thankfully acknowledge the FEDER program for the instrumentation used in this work.

Appendix A. Supplementary data

Supplementary data to this article can be found online at https://doi.org/10.1016/j.atmosenv.2019.116824.

References

Alados-Arboledas, L., Lyamani, H., Olmo, F.J., 2003. Aerosol size properties at Armilla, Granada (Spain). Q. J. R. Meteorol. Soc. 129, 1395–1413. https://doi.org/10.1256/qj.01.207.

Alados-Arboledas, L., Alcántara, A., Olmo, F.J., Martínez-Lozano, J.A., Estellés, V., Cachorro, V., Silva, A.M., Horvath, H., Gangl, M., Díaz, A., Pujadas, M., Lorente, J., Labajo, A., Sorribas, M., Pavese, G., 2008. Aerosol columnar properties retrieved from CIMEL radiometers during VELETA 2002. Atmos. Environ. 42, 2654–2667. https://doi.org/10.1016/j.atmosenv.2007.10.006.

Amiridis, V., Balis, D.S., Kazadzis, S., Bais, A., Giannakaki, E., Papayannis, A., Zerefos, C., 2005. Four year aerosol observations with a Raman lidar at Thessaloniki, Greece, in the framework of European aerosol research lidar network (EARLINET). J. Geophys. Res. Atmos. 110. https://doi.org/10.1029/2005JD006190.

Ansmann, A., Riebesell, M., Wandinger, U., Weitkamp, C., Voss, E., Lahmann, W., Michaelis, W., 1992. Combined Raman elastic-backscatter LIDAR for vertical profiling of moisture, aerosol extinction, backscatter, and LIDAR ratio. Appl. Phys. B 55, 18–28.

Ansmann, A., Petzold, A., Kandler, K., Tegen, I., Wendisch, M., Müller, D., Weinzierl, B., Müller, T., Heintzenberg, J., 2011. Saharan mineral dust experiments SAMUM-1 and SAMUM-2: what have we learned? Tellus Ser. B Chem. Phys. Meteorol. 63, 403–429. https://doi.org/10.1111/j.1600-0889.2011.00555.x.

Atkinson, James D., Murray, Benjamin J., Woodhouse, Matthew T., Whale, Thomas F., Baustian, K.J., et al., 2013. The importance of feldspar for ice nucleation by mineral dust inmixed-phase clouds - ProQuest. Nature 498.

Balis, D.S., Amiridis, V., Nickovic, S., Papayannis, A., Zerefos, C., 2004. Optical properties of Saharan dust layers as detected by a Raman lidar at Thessaloniki, Greece. Geophys.

Res. Lett. 31, 10–13. https://doi.org/10.1029/2004GL019881.
Balis, D., Amiridis, V., Kazadzis, S., Papayannis, A., Tsaknakis, G., Tzortzakis, S., Kalivitis, N., Vrekoussis, M., Kanakidou, M., Mihalopoulos, N., Chourdakis, G., Nickovic, S., Perez, C., Baldasano, J., Drakakis, M., 2006. Optical characteristics of desert dust over the East Mediterranean during summer. Ann. Geophys. 24.
Bauer, S., Bierwirth, E., Esselborn, M., Petzold, A., Macke, A., Trautmann, T., Wendisch, M., 2011. Airborne spectral radiation measurements to derive solar radiative forcing of Saharan dust mixed with biomass burning smoke particles. Tellus Ser. B Chem. Phys. Meteorol. 63, 742–750. https://doi.org/10.1111/j.1600-0889.2011.00567.x.
Benavent-Oltra, J.A., Román, R., Granados-Munõz, M.J., Pérez-Ramírez, D., Ortiz-Amezcua, P., Denjean, C., Lopatin, A., Lyamani, H., Torres, B., Guerrero-Rascado, J.L., Fuertes, D., Dubovik, O., Chaikovsky, A., Olmo, F.J., Mallet, M., Alados-Arboledas, L., 2017. Comparative assessment of GRASP algorithm for a dust event over Granada (Spain) during ChArMEx-ADRIMED 2013 campaign. Atmos. Meas. Tech. 10, 4439–4457. https://doi.org/10.5194/amt-10-4439-2017.
Bergstrom, R.W., Pilewskie, P., Russell, P.B., Redemann, J., Bond, T.C., Quinn, P.K., Sierau, B., 2007. Spectral absorption properties of atmospheric aerosols. Atmos. Chem. Phys. 7, 5937–5943. https://doi.org/10.5194/acp-7-5937-2007.
Böckmann, C., Kirsche, A., 2006. Iterative regularization method for lidar remote sensing. Comput. Phys. Commun. 174, 607–615. https://doi.org/10.1016/j.cpc.2005.12.019.
Böckmann, C., Osterloh, L., 2014. Runge-Kutta type regularization method for inversion of spheroidal particle distribution from limited optical data. Inverse Probl. Sci. Eng. 22, 150–165. https://doi.org/10.1080/17415977.2013.830615.
Böckmann, C., Wandinger, U., Ansmann, A., Bösenberg, J., Amiridis, V., Boselli, A., Delaval, A., De Tomasi, F., Frioud, M., Grigorov, I.V., Hågård, A., Horvat, M., Iarlori, M., Komguem, L., Kreipl, S., Larchevêque, G., Matthias, V., Papayannis, A., Pappalardo, G., Rocadenbosch, F., Rodrigues, J.A., Schneider, J., Shcherbakov, V., Wiegner, M., 2004. Aerosol lidar intercomparison in the framework of the EARLINET project 2 Aerosol backscatter algorithms. Appl. Opt. 43, 977. https://doi.org/10.1364/AO.43.000977.
Böckmann, C., Mironova, I., Müller, D., Schneidenbach, L., Nessler, R., 2005. Microphysical aerosol parameters from multiwavelength lidar. J. Opt. Soc. Am. A 22, 518. https://doi.org/10.1364/JOSAA.22.000518.
Bravo-Aranda, J.A., Navas-Guzmán, F., Guerrero-Rascado, J.L., Pérez-Ramírez, D., Granados-Muñoz, M.J., Alados-Arboledas, L., 2013. Analysis of lidar depolarization calibration procedure and application to the atmospheric aerosol characterization. Int. J. Remote Sens. 34, 3543–3560. https://doi.org/10.1080/01431161.2012.716546.
Bravo-Aranda, J.A., Titos, G., Granados-Muñoz, M.J., Guerrero-Rascado, J.L., Navas-Guzmán, F., Valenzuela, A., Lyamani, H., Olmo, F.J., Andrey, J., Alados-Arboledas, L., 2015. Study of mineral dust entrainment in the planetary boundary layer by lidar depolarisation technique. Tellus Ser. B Chem. Phys. Meteorol. https://doi.org/10.3402/tellusb.v67.26180.
Burton, S.P., Ferrare, R.A., Hostetler, C.A., Hair, J.W., Rogers, R.R., Obland, M.D., Butler, C.F., Cook, A.L., 2012. Aerosol Classification Using Airborne High Spectral Resolution Lidar Measurements – Methodology and Examples 73–98. https://doi.org/10.5194/amt-5-73-2012.
Burton, S.P., Hair, J.W., Kahnert, M., Ferrare, R.A., Hostetler, C.A., Cook, A.L., Harper, D.B., Berkoff, T.A., Seaman, S.T., Collins, J.E., Fenn, M.A., Rogers, R.R., 2015. Observations of the spectral dependence of linear particle depolarization ratio of aerosols using NASA Langley airborne High Spectral Resolution Lidar. Atmos. Chem. Phys. 15, 13453–13473. https://doi.org/10.5194/acp-15-13453-2015.
Córdoba-Jabonero, C., Sorribas, M., Guerrero-Rascado, J.L., Adame, J.A., Hernández, Y., Lyamani, H., Cachorro, V., Gil, M., Alados-Arboledas, L., Cuevas, E., De La Morena, B., 2011. Synergetic monitoring of Saharan dust plumes and potential impact on surface: a case study of dust transport from Canary Islands to Iberian Peninsula. Atmos. Chem. Phys. https://doi.org/10.5194/acp-11-3067-2011.
Cwiertny, D.M., Young, M.A., Grassian, V.H., 2008. Chemistry and Photochemistry of Mineral Dust Aerosol *. https://doi.org/10.1146/annurev.physchem.59.032607.093630.
Denjean, C., Cassola, F., Mazzino, A., Triquet, S., Chevaillier, S., Grand, N., Bourrianne, T., Momboisse, G., Sellegri, K., Schwarzenbock, A., Freney, E., Mallet, M., Formenti, P., 2016. Size distribution and optical properties of mineral dust aerosols transported in the western Mediterranean. Atmos. Chem. Phys. https://doi.org/10.5194/acp-16-1081-2016.
Dubovik, O., King, M.D., 2000. A flexible inversion algorithm for retrieval of aerosol optical properties from Sun and sky radiance measurements. J. Geophys. Res. Atmos. 105, 20673–20696. https://doi.org/10.1029/2000JD900282.
Dubovik, O., Holben, B., Eck, T.F., Smirnov, A., Kaufman, Y.J., King, M.D., Tanré, D., Slutsker, I., 2002. Variability of absorption and optical properties of key aerosol types observed in worldwide locations. J. Atmos. Sci. 59, 590–608. https://doi.org/10.1175/1520-0469(2002)059<0590:VOAAOP>2.0.CO;2.
Dubovik, O., Sinyuk, A., Lapyonok, T., Holben, B.N., Mishchenko, M., Yang, P., Eck, T.F., Volten, H., Muñoz, O., Veihelmann, B., van der Zande, W.J., Leon, J.F., Sorokin, M., Slutsker, I., 2006. Application of spheroid models to account for aerosol particle nonsphericity in remote sensing of desert dust. J. Geophys. Res. Atmos. 111, 1–34. https://doi.org/10.1029/2005JD006619.
Dunion, J.P., Velden, C.S., Dunion, J.P., Velden, C.S., 2004. The impact of the saharan air layer on Atlantic tropical cyclone activity. Bull. Am. Meteorol. Soc. 85, 353–365. https://doi.org/10.1175/BAMS-85-3-353.
Escudero, M., Castillo, S., Querol, X., Avila, A., Alarcón, M., Viana, M.M., Alastuey, A., Cuevas, E., Rodríguez, S., 2005. Wet and dry African dust episodes over eastern Spain. J. Geophys. Res. D Atmos. 110, 1–15. https://doi.org/10.1029/2004JD004731.
Fiedler, S., Schepanski, K., Knippertz, P., Heinold, B., Tegen, I., 2014. How important are atmospheric depressions and mobile cyclones for emitting mineral dust aerosol in North Africa? Atmos. Chem. Phys. 14, 8983–9000. https://doi.org/10.5194/acp-14-8983-2014.
Flaounas, E., Kotroni, V., Lagouvardos, K., Kazadzis, S., Gkikas, A., Hatzianastassiou, N., 2015. Cyclone contribution to dust transport over the Mediterranean region. Atmos. Sci. Lett. 16, 473–478. https://doi.org/10.1002/asl.584.
Forster, P., Ramaswamy, V., Artaxo, P., Berntsen, T., Betts, R., Fahey, D.W., Haywood, J., Lean, J., Lowe, D.C., Myhre, G., Nganga, J., Raga, R.P.,G., Schulz, M., R.V.D, 2007. Changes in atmospheric constituents and in radiative forcing. In: Solomon, S., Qin, D., Manning, M., Chen, Z., Marquis, M., Averyt, K.B., M.T, H.L.M (Eds.), Climate Change 2007: the Physical Science Basis Contribution of Working Group I to the Fourth Assessment Report of the Intergovernmental Panel on Climate Change. Cambridge University Press, Cambridge, United Kingdom and New York, NY, USA.
Freudenthaler, V., 2008. The telecover test: a quality assurance tool for the optical part of a lidar system. In: Proc. 24th International Laser Radar Conference, 23–27 June 2008, Boulder, CO, USA, S01P-3.
Freudenthaler, V., Esselborn, M., Wiegner, M., Heese, B., Tesche, M., Ansmann, A., Müller, D., Althausen, D., Wirth, M., Fix, A., Ehret, G., Knippertz, P., Toledano, C., Gasteiger, J., Garhammer, M., Seefeldner, M., 2009a. Depolarization ratio profiling at several wavelengths in pure Saharan dust during SAMUM 2006. Tellus Ser. B Chem. Phys. Meteorol. 61, 165–179. https://doi.org/10.1111/j.1600-0889.2008.00396.x.
Freudenthaler, V., Esselborn, M., Wiegner, M., Heese, B., Tesche, M., Ansmann, A., Müller, D., Althausen, D., Wirth, M., Fix, A., Ehret, G., Knippertz, P., Toledano, C., Gasteiger, J., Garhammer, M., Seefeldner, M., 2009b. Depolarization ratio profiling at several wavelengths in pure Saharan dust during SAMUM 2006. Tellus Ser. B Chem. Phys. Meteorol. https://doi.org/10.1111/j.1600-0889.2008.00396.x.
Freudenthaler, V., Esselborn, M., Wiegner, M., Heese, B., Tesche, M., Ansmann, A., Muller, D., Althausen, D., Wirth, M., Fix, A., Ehret, G., Knippetz, P., Toledano, C., Gasteiger, J., Garhammer, M., Seefeldner, M., 2009c. Depolarization ratio profiling at several wavelengths in pure Saharan dust during SAMUM 2006. Tellus B 61, 165–179. https://doi.org/10.1111/j.1600-0889.2008.00396.x.
Ganor, E., Osetinsky, I., Stupp, A., Alpert, P., 2010. Increasing trend of African dust, over 49 years, in the eastern Mediterranean. J. Geophys. Res. Atmos. 115, 1–7. https://doi.org/10.1029/2009JD012500.
Gerasopoulos, E., Amiridis, V., Kazadzis, S., Kokkalis, P., Eleftheratos, K., Andreae, M.O., Andreae, T.W., El-Askary, H., Zerefos, C.S., 2011. Three-year ground based measurements of aerosol optical depth over the Eastern Mediterranean: the urban environment of Athens. Atmos. Chem. Phys. 11, 2145–2159. https://doi.org/10.5194/acp-11-2145-2011.
Giannakaki, E., Van Zyl, P.G., Müller, D., Balis, D., Komppula, M., 2016. Optical and microphysical characterization of aerosol layers over South Africa by means of multi-wavelength depolarization and Raman lidar measurements. Atmos. Chem. Phys. 16, 8109–8123. https://doi.org/10.5194/acp-16-8109-2016.
Gkikas, A., Hatzianastassiou, N., Mihalopoulos, N., 2009. Aerosol events in the broader Mediterranean basin based on 7-year (2000-2007) MODIS C005 data. Ann. Geophys. 27, 3509–3522. https://doi.org/10.5194/angeo-27-3509-2009.
Gkikas, A., Houssos, E.E., Lolis, C.J., Bartzokas, A., Mihalopoulos, N., Hatzianastassiou, N., 2015. Atmospheric circulation evolution related to desert-dust episodes over the Mediterranean. Q. J. R. Meteorol. Soc. 141, 1634–1645. https://doi.org/10.1002/qj.2466.
Groß, S., Tesche, M., Freudenthaler, V., Toledano, C., Wiegner, M., Ansmann, A., Althausen, D., Seefeldner, M., 2011a. Characterization of Saharan dust, marine aerosols and mixtures of biomass-burning aerosols and dust by means of multi-wavelength depolarization and Raman lidar measurements during SAMUM 2. Tellus Ser. B Chem. Phys. Meteorol. 63, 706–724. https://doi.org/10.1111/j.1600-0889.2011.00556.x.
Groß, S., Tesche, M., Freudenthaler, V., Toledano, C., Wiegner, M., Ansmann, A., Althausen, D., Seefeldner, M., 2011b. Characterization of Saharan dust, marine aerosols and mixtures of biomass-burning aerosols and dust by means of multi-wavelength depolarization and Raman lidar measurements during SAMUM 2. Tellus Ser. B Chem. Phys. Meteorol. https://doi.org/10.1111/j.1600-0889.2011.00556.x.
Groß, S., Esselborn, M., Weinzierl, B., Wirth, M., Fix, A., P.A, 2013. Aerosol Classification by Airborne High Spectral Resolution Lidar Observations 2487–2505. https://doi.org/10.5194/acp-13-2487-2013.
Groß, S., Freudenthaler, V., Schepanski, K., Toledano, C., Schäfler, A., Ansmann, A., Weinzierl, B., 2015. Optical properties of long-range transported Saharan dust over Barbados as measured by dual-wavelength depolarization Raman lidar measurements. Atmos. Chem. Phys. 15, 11067–11080. https://doi.org/10.5194/acp-15-11067-2015.
Guerrero-Rascado, J.L., Ruiz, B., Alados-Arboledas, L., 2008. Multi-spectral Lidar characterization of the vertical structure of Saharan dust aerosol over southern Spain. Atmos. Environ. 42, 2668–2681. https://doi.org/10.1016/j.atmosenv.2007.12.062.
Guerrero-Rascado, J.L., Olmo, F.J., Avilés-Rodríguez, I., Navas-Guzmán, F., Pérez-Ramírez, D., Lyamani, H., Arboledas, L.A., 2009. Extreme saharan dust event over the southern iberian peninsula in september 2007: active and passive remote sensing from surface and satellite. Atmos. Chem. Phys. https://doi.org/10.5194/acp-9-8453-2009.
Guerrero-Rascado, J.L., Costa, M.J., Bortoli, D., Silva, A.M., Lyamani, H., Alados-Arboledas, L., 2010. Infrared lidar overlap function: an experimental determination. Optic Express 18 20350–9. https://doi.org/10.1364/OE.18.020350.
Hansen, C., 2010. Discrete Inverse Problems: Insight and Algorithms. SIAM.
Holben, B.N., Eck, T.F., Slutsker, I., Tanré, D., Buis, J.P., Setzer, A., Vermote, E., Reagan, J.A., Kaufman, Y.J., Nakajima, T., Lavenu, F., Jankowiak, I., Smirnov, A., 1998. AERONET—a federated instrument network and data archive for aerosol characterization. Remote Sens. Environ. 66, 1–16. https://doi.org/10.1016/S0034-4257(98)00031-5.
Intergovernmental Panel on Climate Change (Ed.), n.d. Clouds and Aerosols, in: Climate

Change 2013 - the Physical Science Basis. Cambridge University Press, Cambridge, pp. 571–658. https://doi.org/10.1017/CBO9781107415324.016.
Kallos, G., 1998. The regional weather forecasting system SKIRON and its capability for forecasting dust up-take and transport. World Meteorol. Organ. TD 157–169.
Kallos, G., Papadopoulos, A., Katsafados, P., Nickovic, S., 2006. Transatlantic Saharan dust transport: model simulation and results. J. Geophys. Res. Atmos. 111, 1–11. https://doi.org/10.1029/2005JD006207.
Karydis, V.A., Tsimpidi, A.P., Bacer, S., Pozzer, A., Nenes, A., Lelieveld, J., 2017. Global impact of mineral dust on cloud droplet number concentration. Atmos. Chem. Phys. 17, 5601–5621. https://doi.org/10.5194/acp-17-5601-2017.
Kim, M., Omar, A.H., Tackett, J.L., Vaughan, M.A., Winker, D.M., Trepte, C.R., Hu, Y., Liu, Z., Poole, L.R., Pitts, M.C., Kar, J., Magill, B.E., 2018. The CALIPSO Version 4 Automated Aerosol Classification and Lidar Ratio Selection Algorithm, vol. 2. pp. 6107–6135.
Knippertz, P., Todd, M.C., 2012. Mineral dust aerosols over the Sahara: meteorological controls on emission and transport and implications for modeling. Rev. Geophys. 50. https://doi.org/10.1029/2011RG000362.
Kokkalis, P., 2017. Using paraxial approximation to describe the optical setup of a typical EARLINET lidar system. Atmos. Meas. Tech. 10, 3103–3115. https://doi.org/10.5194/amt-10-3103-2017.
Kokkalis, P., Papayannis, A., Mamouri, R.E., Tsaknakis, G., Amiridis, V., 2012. The EOLE Lidar System of the National Technical University of Athens. 26th International Laser Radar Conference. June 25-29, 2012, Porto Heli, Greece.
Lopatin, A., Dubovik, O., Chaikovsky, A., Goloub, P., Lapyonok, T., Tanré, D., Litvinov, P., 2013. Enhancement of Aerosol Characterization Using Synergy of Lidar and Sun-Photometer Coincident Observations : the GARRLiC Algorithm 2065–2088. https://doi.org/10.5194/amt-6-2065-2013.
Lyamani, H., Olmo, F.J., Alados-Arboledas, L., 2005. Saharan dust outbreak over south-eastern Spain as detected by sun photometer. Atmos. Environ. 39, 7276–7284. https://doi.org/10.1016/j.atmosenv.2005.09.011.
Lyamani, H., Olmo, F.J., Alcántara, A., Alados-Arboledas, L., 2006a. Atmospheric aerosols during the 2003 heat wave in southeastern Spain I: spectral optical depth. Atmos. Environ. 40, 6453–6464. https://doi.org/10.1016/j.atmosenv.2006.04.048.
Lyamani, H., Olmo, F.J., Alcántara, A., Alados-Arboledas, L., 2006b. Atmospheric aerosols during the 2003 heat wave in southeastern Spain II: microphysical columnar properties and radiative forcing. Atmos. Environ. 40, 6465–6476. https://doi.org/10.1016/j.atmosenv.2006.04.047.
Lyamani, H., Olmo, F.J., Alados-Arboledas, L., 2008. Light scattering and absorption properties of aerosol particles in the urban environment of Granada, Spain. Atmos. Environ. 42, 2630–2642. https://doi.org/10.1016/j.atmosenv.2007.10.070.
Lyamani, H., Olmo, F.J., Alados-Arboledas, L., 2010. Physical and optical properties of aerosols over an urban location in Spain: seasonal and diurnal variability. Atmos. Chem. Phys. 10, 239–254. https://doi.org/10.5194/acp-10-239-2010.
Mamouri, R.E., Ansmann, A., 2015. Estimated desert-dust ice nuclei profiles from polarization lidar: methodology and case studies. Atmos. Chem. Phys. 15, 3463–3477. https://doi.org/10.5194/acp-15-3463-2015.
Matthais, V., Freudenthaler, V., Amodeo, A., Balin, I., Balis, D., Bösenberg, J., Chaikovsky, A., Chourdakis, G., Comeron, A., Delaval, A., De Tomasi, F., Eixmann, R., Hågård, A., Komguem, L., Kreipl, S., Matthey, R., Rizi, V., Rodrigues, J.A., Wandinger, U., Wang, X., 2004. Aerosol lidar intercomparison in the framework of the EARLINET project. 1. Instrum. Appl. Opt. 43, 961–976.
Mattis, I., Ansmann, A., Müller, D., Wandinger, U., Althausen, D., 2002a. Dual-wavelength Raman lidar observations of the extinction-to-backscatter ratio of Saharan dust. Geophys. Res. Lett. 29, 20–21. https://doi.org/10.1029/2002GL014721.
Mattis, I., Ansmann, A., Müller, D., Wandinger, U., Althausen, D., 2002b. Dual-wavelength Raman lidar observations of the extinction-to-backscatter ratio of Saharan dust. Geophys. Res. Lett. https://doi.org/10.1029/2002gl014721.
Mattis, I., Müller, D., Ansmann, A., Wandinger, U., Preißler, J., Seifert, P., Tesche, M., 2008. Ten years of multiwavelength Raman lidar observations of free-tropospheric aerosol layers over central Europe: geometrical properties and annual cycle. J. Geophys. Res. Atmos. 113. https://doi.org/10.1029/2007JD009636.
Mona, L., Amodeo, A., Pandolfi, M., Pappalardo, G., 2006. Saharan dust intrusions in the Mediterranean area: three years of Raman lidar measurements. J. Geophys. Res. Atmos. 111, 1–13. https://doi.org/10.1029/2005JD006569.
Mona, L., Liu, Z., Müller, D., Omar, A., Papayannis, A., Pappalardo, G., Sugimoto, N., Vaughan, M., 2012. Lidar measurements for desert dust characterization: an overview. Adv. Meteorol. 2012. https://doi.org/10.1155/2012/356265.
Müller, D., Ansmann, A., Mattis, I., Tesche, M., Wandinger, U., Althausen, D., Pisani, G., 2007. Aerosol-type-dependent lidar ratios observed with Raman lidar. J. Geophys. Res. Atmos. 112. https://doi.org/10.1029/2006JD008292.
Müller, D., Heinold, B., Tesche, M., Tegen, I., Althausen, D., Arboledas, L.A., Amiridis, V., Amodeo, A., Ansmann, A., Balis, D., Comeron, A., D'amico, G., Gerasopoulos, E., Guerrero-rascado, J.L., Freudenthaler, V., Giannakaki, E., Heese, B., Iarlori, M., Knippertz, P., Mamouri, R.E., Mona, L., Papayannis, A., Pappalardo, G., Perrone, R.M., Pisani, G., Rizi, V., Sicard, M., Spinelli, N., Tafuro, A., Wiegner, M., 2009. EARLINET observations of the 14-22-May long-range dust transport event during SAMUM 2006: validation of results from dust transport modelling. Tellus Ser. B Chem. Phys. Meteorol. 61, 325–339. https://doi.org/10.1111/j.1600-0889.2008.00400.x.
Müller, D., Böckmann, C., Kolgotin, A., Schneidenbach, L., Chemyakin, E., Rosemann, J., Znak, P., Romanov, A., 2016. Microphysical particle properties derived from inversion algorithms developed in the framework of EARLINET. Atmos. Meas. Tech. 9, 5007–5035. https://doi.org/10.5194/amt-9-5007-2016.
Navas-Guzmán, F., Rascado, J.L.G., Arboledas, L.A., 2011. Retrieval of the lidar overlap function using Raman signals. Opt. Pura Apl. 44, 71–75.
Nicolae, D., Nemuc, A., Müller, D., Talianu, C., Vasilescu, J., Belegante, L., Kolgotin, A., 2013. Characterization of fresh and aged biomass burning events using multi-wavelength Raman lidar and mass spectrometry. J. Geophys. Res. Atmos. 118, 2956–2965. https://doi.org/10.1002/jgrd.50324.
Papayannis, A., Ancellet, G., Pelon, J., Mégie, G., 1990. Multiwavelength lidar for ozone measurements in the troposphere and the lower stratosphere. Appl. Opt. 29, 467–476. https://doi.org/10.1364/AO.29.00046760866.
Papayannis, A., Balis, D., Amiridis, V., Chourdakis, G., Tsaknakis, G., Zerefos, C., Castanho, A.D.A., Nickovic, S., Kazadzis, S., Grabowski, J., 2005. Measurements of Saharan dust aerosols over the Eastern Mediterranean using elastic backscatter-Raman lidar, spectrophotometric and satellite observations in the frame of the EARLINET project. Atmos. Chem. Phys. 5, 2065–2079.
Papayannis, A., Amiridis, V., Mona, L., Tsaknakis, G., Balis, D., Bösenberg, J., Chaikovski, A., Tomasi, F. De, Grigorov, I., Mattis, I., Mitev, V., Müller, D., Nickovic, S., Pérez, C., Pietruczuk, A., Pisani, G., Ravetta, F., Rizi, V., Sicard, M., Trickl, T., Wiegner, M., Gerding, M., Mamouri, R.E., D'Amico, G., Pappalardo, G., 2008. Systematic lidar observations of Saharan dust over Europe in the frame of EARLINET (2000–2002). J. Geophys. Res. Atmos. 113. https://doi.org/10.1029/2007JD009028.
Pappalardo, G., Amodeo, A., Apituley, A., Comeron, A., Freudenthaler, V., Linné, H., Ansmann, A., Bösenberg, J., D 'amico, G., Mattis, I., Mona, L., Wandinger, U., Amiridis, V., Alados-Arboledas, L., Nicolae, D., Wiegner, M., 2014. EARLINET: towards an advanced sustainable European aerosol lidar network. Atmos. Meas. Tech. 7, 2389–2409. https://doi.org/10.5194/amt-7-2389-2014.
Pérez, C., Nickovic, S., Baldasano, J.M., Sicard, M., Rocadenbosch, F., Cachorro, V.E., 2006. A long Saharan dust event over the western Mediterranean: lidar, Sun photometer observations, and regional dust modeling. J. Geophys. Res. Atmos. 111, 1–16. https://doi.org/10.1029/2005JD006579.
Petzold, A., Rasp, K., Weinzierl, B., Esselborn, M., Hamburger, T., Dörnbrack, A., Kandler, K., Schütz, L., Knippertz, P., Fiebig, M., Virkkula, A., 2009. Saharan dust absorption and refractive index from aircraft-based observations during SAMUM 2006. Tellus Ser. B Chem. Phys. Meteorol. 61, 118–130. https://doi.org/10.1111/j.1600-0889.2008.00383.x.
Preißler, J., Wagner, F., Pereira, S.N., Guerrero-Rascado, J.L., 2011. Multi-instrumental observation of an exceptionally strong Saharan dust outbreak over Portugal. J. Geophys. Res. Atmos. https://doi.org/10.1029/2011JD016527.
Preißler, J., Wagner, F., Guerrero-Rascado, J.L., Silva, A.M., 2013. Two years of free-tropospheric aerosol layers observed over Portugal by lidar. J. Geophys. Res. Atmos. 118, 3676–3686. https://doi.org/10.1002/jgrd.503502013.
Prospero, J.M., 1996. Saharan dust transport over the North Atlantic Ocean and the mediterranean. In: The Impact of Desert Dust across the Mediterranean. Springer, New York.
Prospero, J.M., Ginoux, P., Torres, O., Nicholson, S.E., Gill, T.E., 2002. Environmental characterization of global sources of atmospheric soil dust identified with the nimbus 7 total ozone mapping spectrometer (TOMS) absorbing aerosol product. Rev. Geophys. 40, 1–2. https://doi.org/10.1029/2000RG000095.
Rolph, G., Stein, A., Stunder, B., 2017. Real-time environmental applications and display sYstem: READY. Environ. Model. Softw 95, 210–228. https://doi.org/10.1016/j.envsoft.2017.06.025.
Rother, T., Kahnert, M., 2009. Electromagnetic Wave Scattering on Nonspherical Particles. https://doi.org/10.1007/978-3-642-00704-0.
Salvador, P., Alonso-Pérez, S., Pey, J., Artíñano, B., De Bustos, J.J., Alastuey, A., Querol, X., 2014. African dust outbreaks over the western Mediterranean Basin: 11-year characterization of atmospheric circulation patterns and dust source areas. Atmos. Chem. Phys. 14, 6759–6775. https://doi.org/10.5194/acp-14-6759-2014.
Samaras, S., 2016. Microphysical Retrieval of Non-spherical Aerosol Particles Using Regularized Inversion of Multi-Wavelength Lidar Data. PhD Thesis. Institut für Mathematik, Numerische Mathematik - Inverse Probleme, University of Potsdam, Germany.
Samaras, S., Nicolae, D., Böckmann, C., Vasilescu, J., Binietoglou, I., Labzovskii, L., Toanca, F., Papayannis, A., 2015. Using Raman-lidar-based regularized microphysical retrievals and Aerosol Mass Spectrometer measurements for the characterization of biomass burning aerosols. J. Comput. Phys. 299, 156–174. https://doi.org/10.1016/j.jcp.2015.06.045.
Sassen, K., 2005. Polarization in lidar. In: C., W (Ed.), Lidar Range-Resolved Optical Remote Sensing of the Atmosphere. Springer, pp. 19–42. https://doi.org/10.1007/978-1-4612-3262-9.
Schepanski, K., Knippertz, P., 2011. Soudano-Saharan depressions and their importance for precipitation and dust: a new perspective on a classical synoptic concept. Q. J. R. Meteorol. Soc. 137, 1431–1445. https://doi.org/10.1002/qj.850.
Schladitz, A., Muller, T., Kaaden, N., Massling, A., Kandler, K., Ebert, M., Weinbruch, S., Deutscher, C., Wiedensohler, A., 2009. In Situ Measurements of Optical Properties at Tinfou (Morocco) during the Saharan Mineral Dust Experiment SAMUM 2006 64–78. https://doi.org/10.1111/j.1600-0889.2008.00397.x.
Schuster, G.L., Dubovik, O., Arola, A., 2016. Remote Sensing of Soot Carbon – Part 1 : Distinguishing Different Absorbing Aerosol Species 1565–1585. https://doi.org/10.5194/acp-16-1565-2016.
Seinfeld, J.H., Bretherton, C., Carslaw, K.S., Coe, H., DeMott, P.J., Dunlea, E.J., Feingold, G., Ghan, S., Guenther, A.B., Kahn, R., Kraucunas, I., Kreidenweis, S.M., Molina, M.J., Nenes, A., Penner, J.E., Prather, K.A., Ramanathan, V., Ramaswamy, V., Rasch, P.J., Ravishankara, A.R., Rosenfeld, D., Stephens, G., Wood, R., 2016. Improving our fundamental understanding of the role of aerosol − cloud interactions in the climate system. Proc. Natl. Acad. Sci. 113, 5781–5790. https://doi.org/10.1073/pnas.1514043113.
Soupiona, O., Papayannis, A., Kokkalis, P., Mylonaki, M., Tsaknakis, G., Argyrouli, A., Vratolis, S., 2018. Long-term systematic profiling of dust aerosol optical properties using the EOLE NTUA lidar system over Athens, Greece (2000–2016). Atmos.

Environ. 183, 165–174. https://doi.org/10.1016/j.atmosenv.2018.04.011.
Stein, A.F., Draxler, R.R., Rolph, G.D., Stunder, B.J.B., Cohen, M.D., Ngan, F., 2015. Noaa's hysplit atmospheric transport and dispersion modeling system. Bull. Am. Meteorol. Soc. 96, 2059–2077. https://doi.org/10.1175/BAMS-D-14-00110.1.
Tesche, M., Gross, S., Ansmann, A., Müller, D., Althausen, D., Freudenthaler, V., Esselborn, M., 2011. Profiling of Saharan dust and biomass-burning smoke with multiwavelength polarization Raman lidar at Cape Verde. Tellus B: Chem. Phys. Meteorol. 63, 649–676. https://doi.org/10.1111/j.1600-0889.2011.00548.x.
Toledano, C., Wiegner, M., Groß, S., Freudenthaler, V., Gasteiger, J., Müller, D., Schladitz, A., Weinzierl, B., Torres, B., O, N.T., Wiegner, M., Groß, S., Freudenthaler, V., Gasteiger, J., Müller, D., Müller, D., Schladitz, A., Weinzierl, B., Torres, B., O'Neill, N.T., 2011. Optical properties of aerosol mixtures derived from sun-sky radiometry during SAMUM-2. Tellus B 63B, 635–648. https://doi.org/10.1111/j.1600-0889.2011.00573.x.
Valenzuela, A., Olmo, F.J., Lyamani, H., Antón, M., Quirantes, A., Alados-Arboledas, L., 2012. Analysis of the columnar radiative properties retrieved during African desert dust events over Granada (2005-2010) using principal plane sky radiances and spheroids retrieval procedure. Atmos. Res. 104–105, 292–301. https://doi.org/10.1016/j.atmosres.2011.11.005.
Valenzuela, A., Olmo, F.J., Lyamani, H., Granados-Muñoz, M.J., Antón, M., Guerrero-Rascado, J.L., Quirantes, A., Toledano, C., Perez-Ramirez, D., A.A.L, 2014a. Aerosol transport over the western Mediterranean basin: evidence of the contribution of fine particles to desert dust plumes over Alborán Island. J. Geophys. Atmos. 119 (14) 028–14,044. https://doi.org/10.1002/2014JD022044.
Valenzuela, A., Olmo, F.J., Lyamani, H., Granados-Muñoz, M.J., Antón, M., Guerrero-Rascado, J.L., Quirantes, A., Toledano, C., Perez-Ramírez, D., Alados-Arboledas, L., 2014b. Aerosol transport over the western mediterranean basin: evidence of the contribution of fine particles to desert dust plumes over alborán island. J. Geophys. Res. https://doi.org/10.1002/2014JD022044.
Veselovskii, I., Goloub, P., Podvin, T., Bovchaliuk, V., Derimian, Y., Augustin, P., Fourmentin, M., Tanre, D., Korenskiy, M., Whiteman, D.N., Diallo, A., Ndiaye, T., Kolgotin, A., Dubovik, O., 2016. Retrieval of optical and physical properties of African dust from multiwavelength Raman lidar measurements during the SHADOW campaign in Senegal. Atmos. Chem. Phys. 16, 7013–7028. https://doi.org/10.5194/acp-16-7013-2016.
Wagner, R., Ajtai, T., Kandler, K., Lieke, K., Linke, C., Muller, T., Schnaiter, M., Vragel, M., 2012. Physics Complex Refractive Indices of Saharan Dust Samples at Visible and Near UV Wavelengths : a Laboratory Study 2491–2512. https://doi.org/10.5194/acp-12-2491-2012.
Wandinger, U., Baars, H., Engelmann, R., Hünerbein, A., Horn, S., Kanitz, T., Donovan, D., van Zadelhoff, G.-J., Daou, D., Fischer, J., von Bismarck, J., Filipitsch, F., Docter, N., Eisinger, M., Lajas, D., Wehr, T., 2016. HETEAC: the aerosol classification model for EarthCARE. EPJ Web Conf. 119, 01004. https://doi.org/10.1051/epjconf/201611901004.
Washington, R., Todd, M., Middleton, N.J., Goudie, A.S., 2003. Dust-storm source areas determined by the total ozone monitoring spectrometer and surface observations. Ann. Assoc. Am. Geogr. 93, 297–313. https://doi.org/10.1111/1467-8306.9302003.
Weinzierl, B., Sauer, D., Esselborn, M., Petzold, A., Veira, A., Rose, M., Mund, S., Wirth, M., Ansmann, A., Tesche, M., Gross, S., Freudenthaler, V., 2011. Microphysical and optical properties of dust and tropical biomass burning aerosol layers in the Cape Verde region-an overview of the airborne in situ and lidar measurements during SAMUM-2. Tellus Ser. B Chem. Phys. Meteorol. https://doi.org/10.1111/j.1600-0889.2011.00566.x.
Zuev, V.V., Burlakov, V.D., Nevzorov, A.V., Pravdin, V.L., Savelieva, E.S., Gerasimov, V.V., 2017. 30-year lidar observations of the stratospheric aerosol layer state over Tomsk (Western Siberia, Russia). Atmos. Chem. Phys. 17, 3067–3081. https://doi.org/10.5194/acp-17-3067-2017.